

Transition of the initial mass function in the metal-poor environments

Sunmyon Chon ¹†, Kazuyuki Omukai ¹, and Raffaella Schneider ^{2,3,4}

¹*Astronomical Institute, Graduate School of Science, Tohoku University, Aoba, Sendai 980-8578, Japan*

²*Dipartimento di Fisica, Università di Roma ‘La Sapienza’, P.le Aldo Moro 2, I-00185 Roma, Italy*

³*INAF/Osservatorio Astronomico di Roma, via di Frascati 33, I-00078 Monteporzio Catone, Italy*

⁴*INFN, Sezione di Roma 1, P.le Aldo Moro 2, I-00185 Roma, Italy*

Accepted 2021. Received 2021; in original form 2021

ABSTRACT

We study star cluster formation in a low-metallicity environment using three dimensional hydrodynamic simulations. Starting from a turbulent cloud core, we follow the formation and growth of protostellar systems with different metallicities ranging from 10^{-6} to $0.1 Z_{\odot}$. The cooling induced by dust grains promotes fragmentation at small scales and the formation of low-mass stars with $M_* \sim 0.01\text{--}0.1 M_{\odot}$ when $Z/Z_{\odot} \gtrsim 10^{-5}$. While the number of low-mass stars increases with metallicity, the stellar mass distribution is still top-heavy for $Z/Z_{\odot} \lesssim 10^{-2}$ compared to the Chabrier initial mass function (IMF). In these cases, star formation begins after the turbulent motion decays and a single massive cloud core monolithically collapses to form a central massive stellar system. The circumstellar disk preferentially feeds the mass to the central massive stars, making the mass distribution top-heavy. When $Z/Z_{\odot} = 0.1$, collisions of the turbulent flows promote the onset of the star formation and a highly filamentary structure develops owing to efficient fine-structure line cooling. In this case, the mass supply to the massive stars is limited by the local gas reservoir and the mass is shared among the stars, leading to a Chabrier-like IMF. We conclude that cooling at the scales of the turbulent motion promotes the development of the filamentary structure and works as an important factor leading to the present-day IMF.

Key words: (stars:) formation – stars: Population II – (stars:) binaries: general

1 INTRODUCTION

The initial mass function (IMF) plays a crucial role in the formation and evolution of the stars and galaxies that we observe today. In the primordial and low-metallicity environments the nature of the IMF is still poorly understood, which limits our knowledge about early structure formation. Among a spectrum of stellar masses, massive stars dramatically change the surrounding environment: they scatter the heavy elements around when they explode as supernovae (Wise et al. 2012; Ritter et al. 2015; Graziani et al. 2015, 2017; Sluder et al. 2016; de Bannassuti et al. 2017; Chiaki et al. 2018) and emit a large amount of ionizing photons that ionize the surrounding gas (Johnson et al. 2013; Chon & Latif 2017; Nakatani et al. 2020). The extremely massive stars ($40 < M_*/M_{\odot} < 120$ or $260 < M_*/M_{\odot}$) directly collapse into the black holes (BHs, e.g. Heger & Woosley 2002), providing a potential formation channel to the seeds of the observed supermassive BHs (e.g. Hosokawa et al. 2012; Latif et al. 2013; Chon et al. 2016; Valiante et al. 2016; Regan et al. 2017; Wise et al. 2019; Inayoshi et al. 2020) and also contributing to cosmic reionization as additional UV radiation

is emitted when the mass falls onto the BHs (e.g. Johnson & Bromm 2007; Alvarez et al. 2009; Johnson et al. 2011; Jeon et al. 2012; Aykutalp et al. 2013, 2014; Chon et al. 2021).

Recent numerical simulations have revealed that the first stars or population III (Pop III) stars are typically massive, with masses in the range $10\text{--}100 M_{\odot}$ (Omukai & Nishi 1998; Bromm et al. 2001; Omukai & Palla 2003; Yoshida et al. 2008; Hosokawa et al. 2011; Hirano et al. 2014, 2015; Susa et al. 2014; Hosokawa et al. 2016; Sugimura et al. 2020), accompanied by a small number of low-mass stars (Machida et al. 2008b; Clark et al. 2011; Greif et al. 2012; Machida & Doi 2013; Stacy et al. 2016; Susa 2019). The Pop III mass spectrum at the lower-mass end is constrained by the number density of metal-poor stars observed in Galactic halo and local dwarf galaxies, indicating a top-heavy IMF in the primordial environments (Salvadori et al. 2007, 2008; de Bannassuti et al. 2014, 2017; Graziani et al. 2015; Ishiyama et al. 2016; Hartwig et al. 2018; Magg et al. 2018). In contrast, observational studies of the IMF in the present-day universe have shown that present-day stars typically have small masses (e.g. Salpeter 1955; Kroupa 2002; Chabrier 2003). The observationally derived IMF has a universal distribution, showing little environmental dependence, and is peaked at $0.1 M_{\odot}$.

† E-mail: sunmyon.chon@astr.tohoku.ac.jp

Still, what drives such transitions, from the top-heavy to the present-day IMF, remains unresolved today.

Thermal processes inside a cloud can determine the typical fragmentation scales of the collapsing cloud and thus give a typical mass of the stars (Larson 1985, 2005; Bonnell et al. 2006). The cloud becomes highly filamentary and starts to fragment when cooling is efficient and the effective specific heat ratio γ is smaller than unity, where $\gamma \equiv d \log P / d \log \rho$ and P and ρ are gas pressure and density, respectively (e.g. Inutsuka & Miyama 1992; Li et al. 2003; Jappsen et al. 2005). Once γ becomes larger than unity, the growth of such filamentary modes ceases and further fragmentation is suppressed, setting a minimum scale for fragmentation.

The presence of metals significantly alters the thermal evolution of the cloud, reducing the gas temperature and the characteristic mass of the stars. The abundance of metals in the gas phase and locked in dust grains is thus thought to be one of the key parameters which drives the IMF transition (e.g. Omukai 2000; Schneider et al. 2003; Omukai et al. 2005; Schneider et al. 2006; Schneider & Omukai 2010; Schneider et al. 2012; Chiaki et al. 2014). In recent three-dimensional simulations, cloud fragmentation is observed when the cloud is enriched to a finite metallicity (Clark et al. 2008; Dopcke et al. 2011, 2013; Safraneck-Shrader et al. 2016; Chiaki et al. 2016; Chiaki & Yoshida 2020). They find that a number of low-mass stars with $M_* \lesssim 0.01\text{--}0.1 M_\odot$ form due to the fragmentation induced by the efficient cooling by dust grains. Even a trace amount of dust with the dust-to-gas mass ratio of $10^{-9} - 10^{-8}$ (which is 10^{-6} times the solar neighborhood value) can trigger the formation of low-mass stars (Schneider et al. 2012).

So far, the stellar mass distribution derived for low-metallicity environments cannot be interpreted as the IMF. Most of the previous studies do not follow the stellar mass evolution for a sufficiently long time-scale, $10^4 - 10^5$ years, nor do not adequately resolve the spatial scales for fragmentation. Since stars are still accreting gas at the end of the simulations, there is still the possibility that massive stars efficiently grows more massive, leading to a top-heavy IMF. For example, Dopcke et al. (2013) followed the evolution only for 120 yrs from the formation of the first protostar, which is not enough to discuss the final IMF shape. Star cluster formation in the present-day universe suggests that massive stars grow in mass while the continuous formation of low-mass stars keeps the shape of the mass function unchanged (e.g. Bate et al. 2003).

Another difficult issue for star formation in low-metallicity environments is that the initial conditions are poorly constrained. Along with cosmic structure formation, not only the metallicity but other important factors evolve with time. The evolution of the abundance pattern of metals or the composition of dust grains (Schneider et al. 2012; Chiaki et al. 2016; Chiaki & Yoshida 2020), heating by the warmer cosmic microwave background (CMB) at high redshift (Smith & Sigurdsson 2007; Jappsen et al. 2009; Schneider & Omukai 2010; Meece et al. 2014; Bovino et al. 2014; Safraneck-Shrader et al. 2014; Riaz et al. 2020), the strength of the turbulent motion induced by the expansion of H II regions or by SN explosions (Smith et al. 2015; Chiaki et al. 2018), and the effects of the magnetic fields generated at some cosmic evolutionary stages (Machida et al. 2009; Machida & Nakamura 2015; Higuchi et al. 2018). While these points are important to fully un-

derstand the star formation process during the evolution of cosmic structures, they are tangled up making it difficult to capture the metallicity effect on the stellar mass distribution.

In this paper, we perform high resolution hydrodynamics simulations following the gravitational collapse of a turbulent cloud core simultaneously solving non-equilibrium chemical reaction network and the associated cooling processes. In order to capture the mass spectra in low-metallicity environments, the simulations resolve the protostellar \sim au scale and extend for $10^4\text{--}10^5$ years, which is a typical time-scale for star formation. We perform the runs assuming six different metallicity values with $10^{-6} \lesssim Z/Z_\odot \lesssim 0.1$, starting from the same initial conditions. This allows us to evaluate impact of the metallicity on the resulting stellar mass distribution. This is the first systematic attempt to investigate how the IMF evolves from the primordial to present-day environments by means of detailed numerical simulations.

This paper is organized as follows. In Section 2, we describe the initial conditions and our numerical methodology. Section 3 presents our numerical results. We discuss the implication of our results and some caveats in Section 4. Concluding remarks are given in Section 5.

2 METHODOLOGY

We perform hydrodynamics simulations using the smoothed particle hydrodynamic (SPH) code, **Gadget-2** (Springel 2005). Starting from an initial turbulent cloud core, we follow the cloud evolution, from the onset of cloud collapse to the formation of numerous protostars. Deriving the protostellar mass functions for different cloud metallicities, we focus on how the cloud metallicity modifies the cloud evolution and thus the mass function of the stars. Here, we describe the initial conditions and overview the numerical methodology additionally implemented into the original version of **Gadget-2** code.

As the initial conditions, we generate the gravitationally unstable critical Bonnor-Ebert sphere, which is characterized by the central gas density n_c and temperature T_c . We take $n_c = 10^4 \text{ cm}^{-3}$ and $T_c = 200 \text{ K}$, which sets the cloud radius to be 1.85 pc. We then enhance the cloud density by a factor of 1.4 to promote gravitational collapse of the cloud, which results in a total cloud mass of $1950 M_\odot$. We employ 4.04×10^6 SPH particles to construct the initial gas sphere, where the particle mass is $4.8 \times 10^{-4} M_\odot$.

We also include rotational and turbulent motions to model the initial velocity field. The turbulent velocity field is generated following Mac Low (1999). We divide the whole simulated region using a 128^3 grid and assign a random velocity component to each grid cell, assuming it follows a random Gaussian fluctuation with a power-law power spectrum, $P(k) \propto k^{-4}$. We then provide each gas particle with a turbulent velocity, interpolating it from the values in the surrounding grid cells (e.g. cloud-in-cell interpolation). We impose transonic turbulence with $M_{\text{ch}} \equiv v_{\text{rms}}/c_s = 1$, where M_{ch} is the Mach number, v_{rms} is the root mean square of the turbulent velocity, and c_s is the sound speed of the gas with temperature T_c . This gives $v_{\text{rms}} = 1.17 \text{ km s}^{-1}$, similar to the turbulent velocity observed in local molecular clouds at pc scale. (Larson 1981; Heyer & Brunt 2004). We also impose rigid rotation on the $x-y$ plane so that the rotational energy

equals 0.1% of the total gravitational energy, which roughly corresponds to the observed rotational energy of the molecular cloud cores, which is in the range $10^{-4} - 0.07$ (Caselli et al. 2002).

During the gravitational collapse of the cloud core, we must be capable of resolving the local Jeans mass M_J with more than 100–1000 particles (e.g. Bate et al. 1995; Truelove et al. 1997; Stacy et al. 2013). For this purpose, once the gas density exceeds 10^6 cm^{-3} , we split each gas particle into 13 daughter particles following the method presented in Kitsionas & Whitworth (2002). The mass of each new particle is thus $3.7 \times 10^{-5} M_\odot$, leading to the minimum resolvable mass scale $M_{\text{res}} \sim 1.5 N_{\text{neigh}} m_{\text{SPH}} = 3.6 \times 10^{-3} M_\odot$, where $N_{\text{neigh}} = 64$ is the number of the neighbour particles and m_{SPH} is the mass of an SPH particle (Bate & Burkert 1997). This allows us to resolve the Jeans mass of cloud cores throughout our simulation, which has $0.01 M_\odot$ at its minimum (e.g. Bate 2009, 2019).

Once the gas density exceeds the critical value n_{sink} , we introduce a sink particle, assuming that a protostar forms inside the cloud core. We set $n_{\text{sink}} = 2.5 \times 10^{16} \text{ cm}^{-3}$ for the following reason. Below this density, the cloud is in hydrostatic equilibrium since the cloud is optically thick and supported by the pressure. Once the cloud density exceeds n_{sink} , owing to the evaporation of dust grains and the chemical cooling caused by H_2 destruction, the cloud starts to collapse onto the protostellar core, which is similar to the second collapse observed in the solar metallicity case (Larson 1969; Masunaga & Inutsuka 2000). In reality, the gravitational collapse further continues until the density reaches $\sim 10^{20} \text{ cm}^{-3}$. Since resolving the formation of protostellar cores is computationally expensive, we introduce the sink particles and mask out the high density region around the protostars, which allows us to follow the formation of the stellar clusters for ~ 0.1 million years. We set the sink radius to be 1 au. Once the gas particles enter the region inside the sink radius, they are assimilated to the sink particle. We allow the merger of a sink particle pair if their separation becomes smaller than the sum of the sink radii.

2.1 Chemistry

We solve non-equilibrium chemical network for 8 species (e^- , H, H^+ , H_2 , H^- , D, D^+ , and HD) and solve the associated cooling/heating processes. The line cooling rates due to rovibrational transition of H_2 and HD molecules are given by

$$\Lambda_{\text{line}} = \beta_{\text{esc}} \Lambda_{\text{thin}} e^{-\tau}, \quad (1)$$

where β_{esc} is the escape probability of the line emission, Λ_{thin} is the line cooling rate in the optically-thin case, and τ is the optical depth of the continuum radiation. We adopt fitted values of Λ_{thin} given by Glover (2015) for H_2 and by Lipovka et al. (2005) for HD and β_{esc} by Fukushima et al. (2018). We consider continuum cooling owing to the primordial species for the following six processes, H free-bound, H free-free, H^- free-free, H^- free-bound, and collision induced emission (CIE) of H_2 - H_2 and H_2 -He (Mayer & Duschl 2005; Matsukoba et al. 2019). We also include chemical heating/cooling associated with the formation/destruction of H_2 .

To model cooling associated with heavy elements, we consider the atomic line transitions of C II and O I and dust thermal emission. We assume that the abundance ratio of heavy

elements and their fraction in the gas and dust phases follow those in the solar neighborhood. The amount of metals and dust are linearly scaled with a given metallicity Z/Z_\odot . We use the dust opacity model given by Semenov et al. (2003), where the composition and the size distribution of dust grains are the same as those found in the solar neighborhood. We compute the dust temperature T_{gr} from the thermal balance between heating and cooling of the dust grains, solving the following equation,

$$4\sigma T_{\text{gr}}^4 \kappa_{\text{gr}} = \Lambda_{\text{gas, dust}} + 4\sigma T_{\text{rad}}^4 \kappa_{\text{gr}}, \quad (2)$$

where σ is the Stefan-Boltzmann constant, κ_{gr} is the opacity of the dust, T_{rad} is the radiation temperature which is set to be the CMB temperature at $z = 0$ (2.72 K), and $\Lambda_{\text{gas, dust}}$ is the energy transfer between the gas and the dust grains due to the collisions, which is taken from Hollenbach & McKee (1979).

Here, we assume all the C and O in the gas phase are in the form of C II and O I and calculate the cooling rate by the fine-structure lines. While the formation of molecules, such as CO, OH, and H_2O , changes the chemical composition and thus slightly modifies the thermal evolution at intermediate metallicity cases $Z/Z_\odot \sim 10^{-4}$ (Omukai et al. 2005; Chiaki et al. 2016), the overall temperature evolution can be adequately described by our simple treatment. In fact, one-zone calculation by Omukai et al. (2005) have shown that this model approximately reproduces the thermal evolution of low-metallicity clouds solved with the full non-equilibrium chemical network of C and O bearing species, within the error of less than 30% in temperature.

3 RESULTS

3.1 Chemo-thermal evolution of the collapsing cloud

We follow the collapse of a turbulent cloud core with different gas metallicities starting from the same initial conditions. The top panel of Fig. 1 shows the density distribution at the moment when the first protostar is formed. When $Z/Z_\odot = 10^{-1}$, filamentary structures develop due to the initial turbulent motion. Such structures become less evident with decreasing metallicity. When $Z/Z_\odot = 10^{-2}$, the density distribution at $n \lesssim 10^5 \text{ cm}^{-3}$ is similar to the case of $Z/Z_\odot = 10^{-1}$, while the density fluctuation seeded by the turbulent motion has dissipated at $n \gtrsim 10^6 \text{ cm}^{-3}$. When $Z/Z_\odot \lesssim 10^{-4}$, the turbulent motion almost completely decays at the epoch of protostar formation. In this case, a massive dense core forms at the cloud center, in which the rotational motion dominates over the turbulence to create a disk-like structure.

The key factor that distinguishes whether the filamentary structure develops is the efficiency of cooling in the shock compressed region. If the turbulent motion becomes converging at some point, the gas density increases due to shock compression, seeding a large density fluctuation. When the shock compressed gas efficiently cools, it can condense further and the protostar forms once the gravitational instability operates therein. The bottom panel of Fig. 1 shows the temperature distribution. The cloud temperature decreases with increasing metallicity, as the cooling becomes more efficient. If we compare the temperature distribution between $Z/Z_\odot = 10^{-1}$ and 10^{-2} cases, the temperature along the

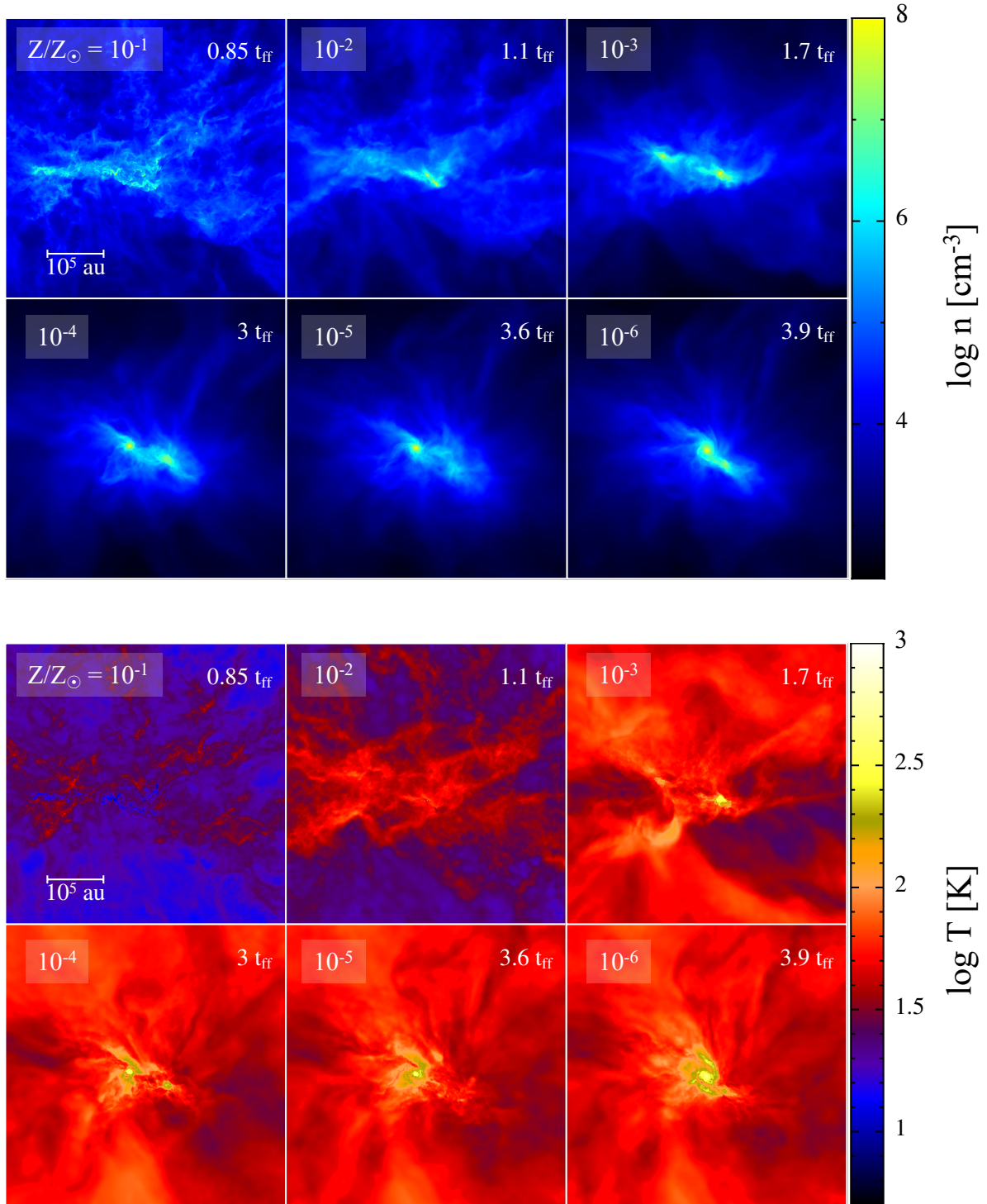


Figure 1. The projected density (top) and temperature distribution (bottom) along the z -axis at the moment when the first protostar forms for the different metallicity cases. We show the corresponding time of the snapshots in the right-top corner of each panel, where t_{ff} is the free-fall time of the initial cloud core.

filamentary region becomes higher in the lower metallicity case. This strengthens the pressure support of the shock compressed region, which counteracts shock-compression and the contraction due to the self-gravity delaying the onset of star formation. The turbulent motion is thus thermalized and quickly decays in the lower metallicity cases. We can also

see that the onset of star formation is delayed as the metallicity decreases. The first protostar formation takes place at $t = 0.85t_{\text{ff}}$ when $Z/Z_{\odot} = 10^{-1}$, while it takes place at $t = 3.9t_{\text{ff}}$ when $Z/Z_{\odot} = 10^{-6}$. The decay of the turbulent motion allows more mass to accumulate at the center and a massive gas disk develops.

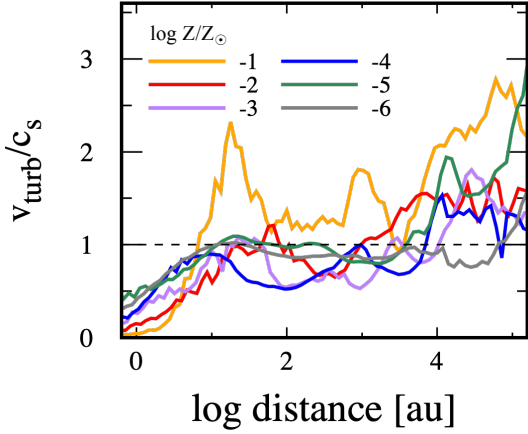


Figure 2. The radial profiles of the turbulent Mach number v_{turb}/c_s for different metallicity values, with $\log Z/Z_{\odot} = -1$ (yellow), -2 (red), -3 (purple), -4 (blue), -5 (green), and -6 (grey line). The black dashed line represents the trans-sonic turbulence with $v_{\text{turb}}/c_s = 1$.

Fig. 2 shows the radial profile of the turbulent Mach number v_{turb}/c_s at the time of formation of the first protostar for each case. Here, the turbulent velocity is defined as the remainder after subtracting non-turbulent motion, i.e., the radial and circular motions, which are respectively caused by the gravitational collapse and initial cloud rotation, from the actual velocity field. To do this, we define the radial and circular motion at each mass shell at the given radius. The radial and circular velocities are defined as the velocity toward the cloud center and that around the rotation axis, respectively. The orientation of the rotation axis is chosen to be that of the angular momentum vector at each mass shell. In Fig. 2 we average the turbulent velocity in the spherical shell at a given distance from the cloud center. When $Z/Z_{\odot} \lesssim 10^{-3}$, the turbulent motion is sub- or trans-sonic inside 10^4 au, while it becomes super-sonic at outer radii. This causes a filamentary and axisymmetric structures in regions of low density as seen in Fig. 1 at a few 10^4 au from the cloud center. When $Z/Z_{\odot} = 10^{-2}$, the turbulence enters the super-sonic regime on scales $r \gtrsim 10^3$ au, much smaller than at lower metallicity. We can see this turbulent motion creates a filamentary structure in the central dense core in Fig. 1. When $Z/Z_{\odot} = 10^{-1}$, the turbulent velocity becomes super-sonic already at $r \gtrsim 10$ au. This means that the turbulent motion cascades toward much smaller scales than in the lower metallicity cases.

Fig. 3 shows the density versus temperature diagrams for the different metallicities at the onset of star formation. We can again see the general trend that the gas temperature decreases with metallicity. The solid line shows the temperature evolution obtained from one-zone calculations, where the cloud collapse is assumed to proceed at the rate of the free-fall time t_{ff} , i.e. $\dot{\rho}/\rho = 1/t_{\text{ff}}$, where ρ is the density and $\dot{\rho}$ is the time derivative of the density. Comparing the cloud temperature with those obtained by the one-zone models, we can understand how turbulence changes the temperature evolution. Turbulence affects the gas temperature in different ways depending on metallicity: the gas temperature increases when $Z/Z_{\odot} \gtrsim 10^{-3}$, while it decreases when

$Z/Z_{\odot} \lesssim 10^{-4}$. In the higher metallicity cases, shock heating results in higher temperature at $n \lesssim 10^6 \text{ cm}^{-3}$. On the other hand, when $Z/Z_{\odot} \lesssim 10^{-4}$, the gas has lower temperature at $n \lesssim 10^8 \text{ cm}^{-3}$ since the turbulence delays the cloud collapse and gives the gas more time to cool, lowering the cloud temperature compared to that in the one-zone model. The temperature evolution almost converges to those in the one-zone model at $n \gtrsim 10^8 \text{ cm}^{-3}$ at any metallicity.

Note that when $Z/Z_{\odot} = 10^{-4}$ and 10^{-5} , the temperature is slightly higher than that expected from the one-zone model in the density range $n \sim 10^{12}\text{--}10^{14} \text{ cm}^{-3}$, where the gas temperature is determined by the balance between the dust cooling and the adiabatic heating. In our simulations, the collapse indeed proceeds faster than the free-fall time assumed in the one-zone model (by a factor 1.5–2 at $n \gtrsim 10^{10} \text{ cm}^{-3}$), leading to higher adiabatic heating rate and thus higher temperature than in the one-zone model.

Fig. 4 shows the time evolution of the cooling/heating rates at the cloud center as a function of the central density n for different metallicities. Shown are the cooling/heating rates averaged over the region within the Jeans length from the cloud center. In the high metallicity cases of $Z/Z_{\odot} = 10^{-1}$ and 10^{-2} , cooling is dominated by the C II and O I fine-structure line cooling in the low-density regime where $n \lesssim 10^6 \text{ cm}^{-3}$, while, with metallicity $Z/Z_{\odot} \lesssim 10^{-3}$, HD cooling dominates over the less efficient metal cooling. The HD abundance, which is determined by the balance of the following two reactions,



becomes higher at lower temperature. Although the H_2 abundance is lower for the lower metallicity gas due to the smaller contribution by the dust-catalyzed formation reaction, the temperature evolution at low densities, where H_2 is the dominant coolant, does not show a strong dependence on metallicity. This is because delayed collapse due to inefficient cooling at low metallicity lowers the adiabatic heating rate, allowing a longer time for H_2 formation, which enhances the cooling rate. Once the temperature falls below $\lesssim 150\text{K}$, most of D is locked up in HD and the gas cools down further to several tens of K by HD cooling. This occurs for all the metallicities in our calculation unlike in the one-zone model in which the collapse rate does not depend on the cooling rate (e.g. Omukai et al. 2005). We can in fact see that the temperature distribution is similar at $n \lesssim 10^8 \text{ cm}^{-3}$ for all the $Z/Z_{\odot} \lesssim 10^{-3}$ models. This also explains why the gas temperature for $Z/Z_{\odot} \lesssim 10^{-3}$ becomes much smaller than that obtained by the one-zone calculation, where HD is not formed efficiently due to the assumption of the short free-fall collapse time-scale. (e.g. Ripamonti 2007; Hirano et al. 2014; Chiaki & Yoshida 2020).

Once the density becomes $n \gtrsim 10^5\text{--}10^6 \text{ cm}^{-3}$, the cooling rates by fine-structure and molecular lines become inefficient as the level population approaches the local thermodynamic equilibrium. When $Z/Z_{\odot} = 10^{-1}$ and 10^{-2} , temperature evolves almost isothermally with ~ 10 K by dust thermal emission until it becomes optically thick at $n \gtrsim 10^{10} \text{ cm}^{-3}$. When $Z/Z_{\odot} \lesssim 10^{-3}$, the temperature increases up to a few 100 K at $n \sim 10^8 \text{ cm}^{-3}$ due to the H_2 formation heating. This is initially balanced by H_2 cooling but soon after the cooling by dust thermal emission dominates, causing the temperature

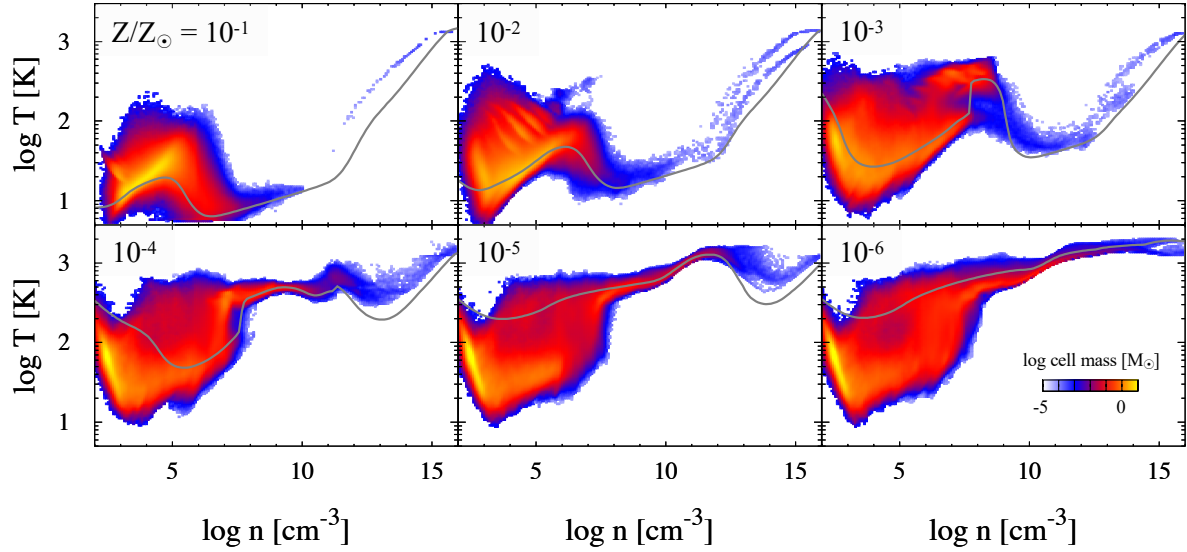


Figure 3. The temperature versus density diagram at the time of formation of the central protostar for the different metallicity models. Colors show the cell mass, where we divide the temperature and density region by 200×200 cells and calculate the gas mass inside each cell. Solid grey lines show the temperature evolution obtained by one-zone calculation with the same metallicity.

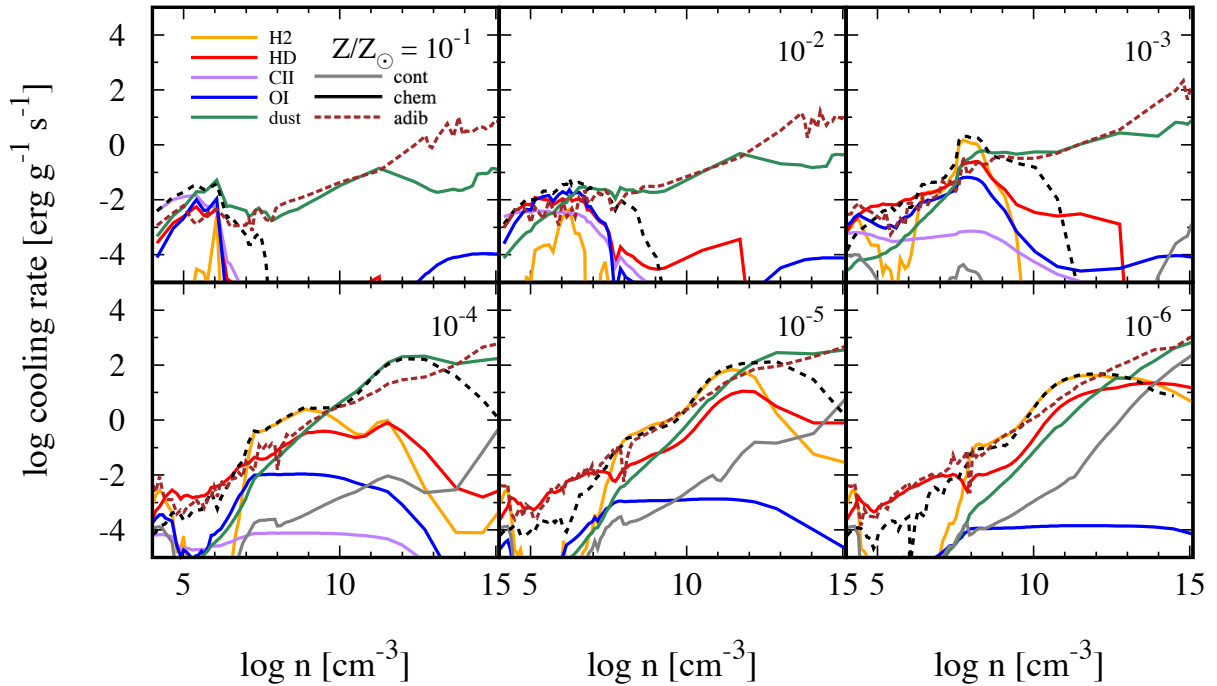


Figure 4. Cooling and heating rate at the cloud center as a function of the central gas density for different metallicity models. The lines with different colors show the cooling and heating rates by H_2 (yellow), HD (red), C II (purple), O I (blue), dust thermal emission (green), continuum process (grey), chemical process (black), and adiabatic compression (brown). The solid and the dashed lines show the cooling and the heating rate, respectively.

evolution minima when the central density is around $10^{10} - 10^{14} \text{ cm}^{-3}$.

Note that we have here neglected the formation of molecules such as CO, OH, and H_2O , and the associated cooling, which becomes important when $Z/Z_\odot = 10^{-4} - 10^{-3}$ (e.g. Omukai et al. 2005; Chiaki et al. 2016). Cooling by such

molecular lines becomes important at $n \sim 10^6 \text{ cm}^{-3}$ and slightly modifies the temperature around this density.

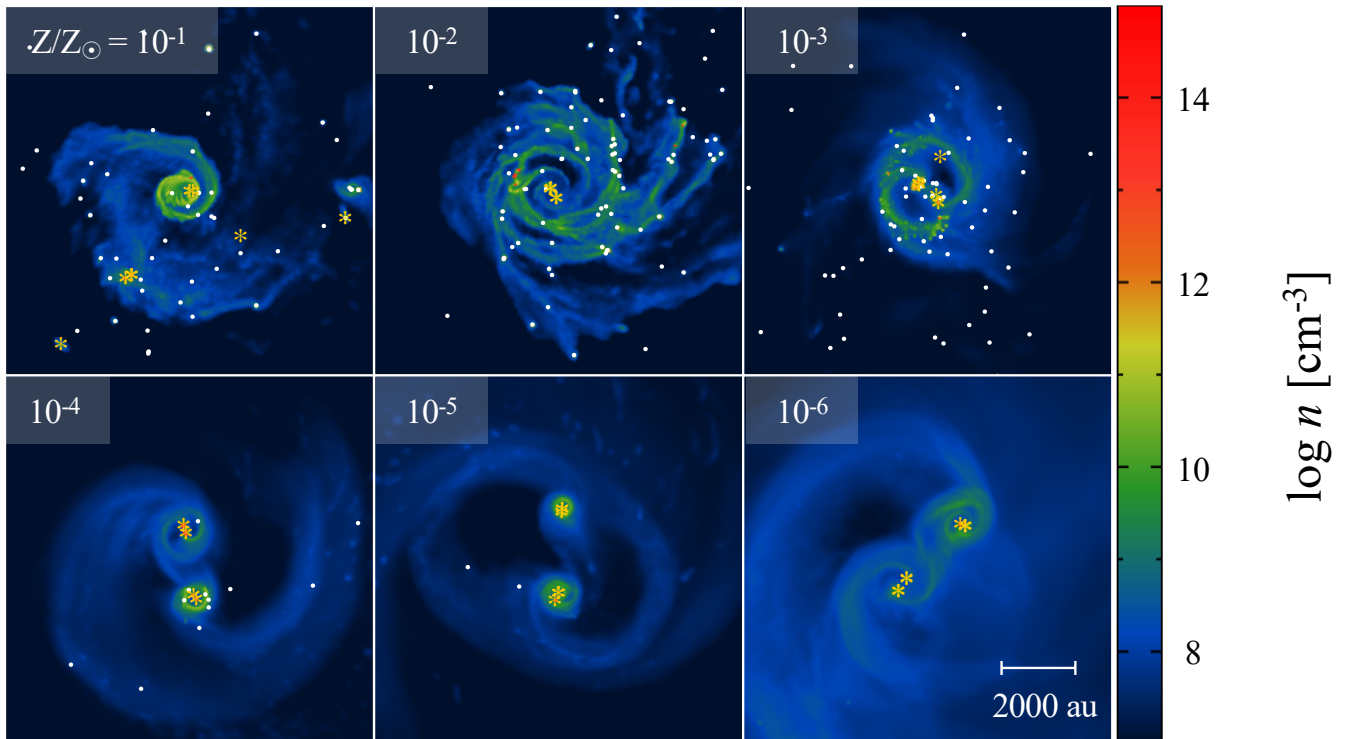
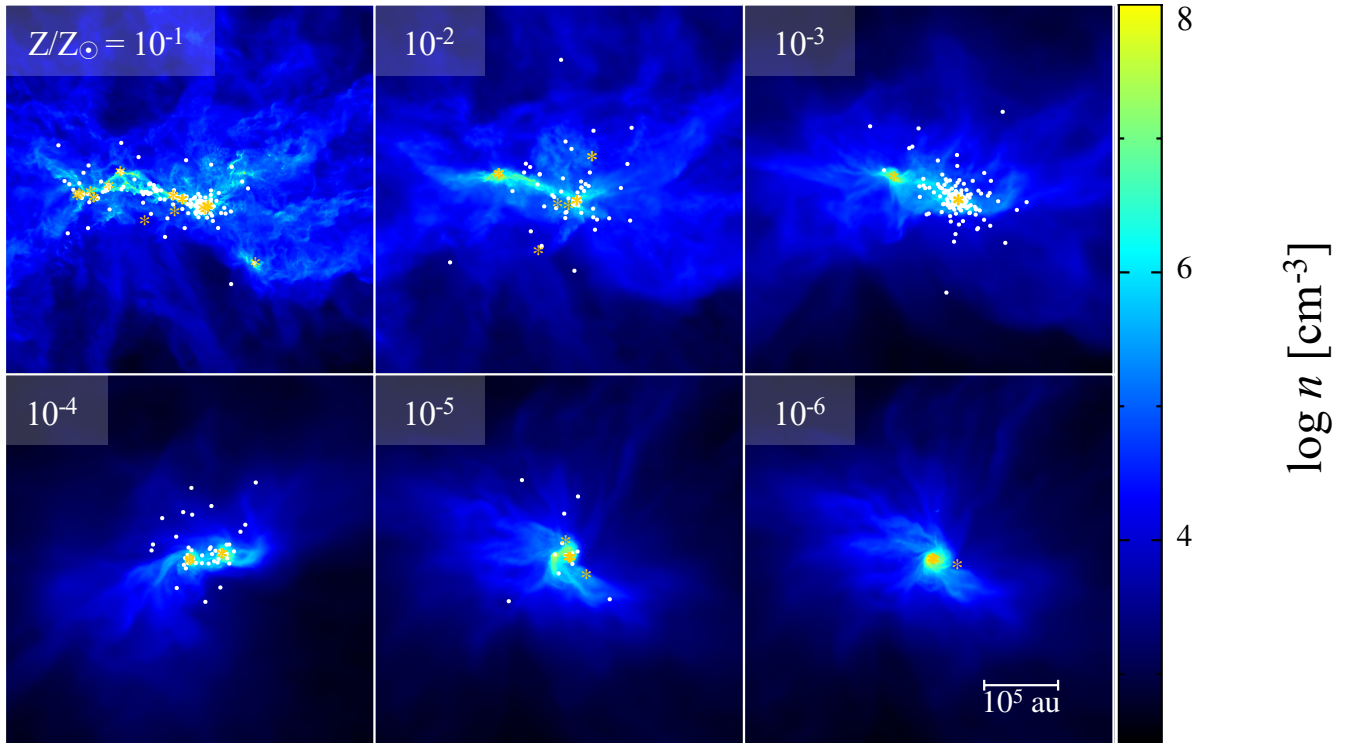


Figure 5. Top: the projected density distribution along z -axis when the total stellar mass reaches $150 M_{\odot}$ for different metallicity models. Yellow asterisks and white dots represent stars with masses larger than and smaller than $1 M_{\odot}$, respectively. Bottom: at the same epoch, the face-on view of the disks around the most massive stars or multiple stellar system.

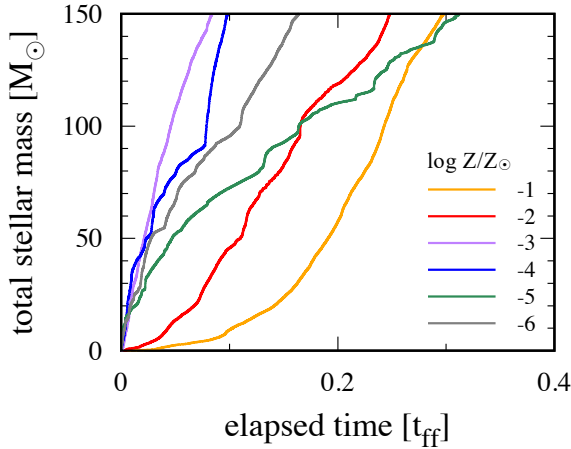


Figure 6. Time evolution of the total stellar mass M_{tot} for $\log Z/Z_{\odot} = -1$ (yellow), -2 (red), -3 (purple), -4 (blue), -5 (green), and -6 (grey). We set the time origin to be the time when the first protostar forms in the cloud. Time is normalized by the free-fall time t_{ff} of the initial cloud core, where $t_{\text{ff}} = 4.7 \times 10^5 \text{ yr}$.

3.2 Formation and evolution of the protostellar system

After the onset of star formation, a number of protostars are formed in the course of our simulation. The top panels of Fig. 5 show the positions of the protostars for the different metallicities, overplotted on the density distribution when in each simulation the total protostellar mass reaches $150 M_{\odot}$. Protostars with masses larger (smaller) than $1 M_{\odot}$ are indicated with yellow asterisks (white dots, respectively). When the metallicity is $0.1 Z_{\odot}$, the turbulent motion induces the formation of a filamentary structure, which fragments into protostars by gravitational instability. At this metallicity, the filament vigorously fragments into small clumps, allowing the formation of protostars throughout the scale of the cloud core. As the metallicity decreases, however, a filamentary structure can hardly develop since the turbulent motion decays due to inefficient cooling. This makes the formation sites of the protostars more concentrated.

The bottom panels of Fig. 5 show the density distribution around the most massive protostars. Here, we determine the orientation of the rotation axis around the most massive protostar by calculating the angular momentum of the gas with $n > 10^8 \text{ cm}^{-3}$ and show the face-on view of the gas distribution around the protostars. We can see that a circumstellar disk forms at all values of the metallicity, while the density structures are very different. When the metallicity is smaller than $10^{-4} Z_{\odot}$, the gas disk surrounds the central massive binary or the multiple stellar system, which is gravitationally stable at this epoch. In these systems, gravitational instability recurrently operates when the disk becomes massive owing to mass accretion from the envelope, which induces fragmentation. The fragment grows in mass via accreting the surrounding gas and grows into massive protostars. As a result, hierarchical binary systems form as seen in simulations of star formation in primordial environments (Chon et al. 2018; Chon & Hosokawa 2019; Susa 2019; Sugimura et al. 2020). The effect of dust thermal emission is only seen very close to the massive protostars within $\lesssim 100 \text{ au}$, which produces

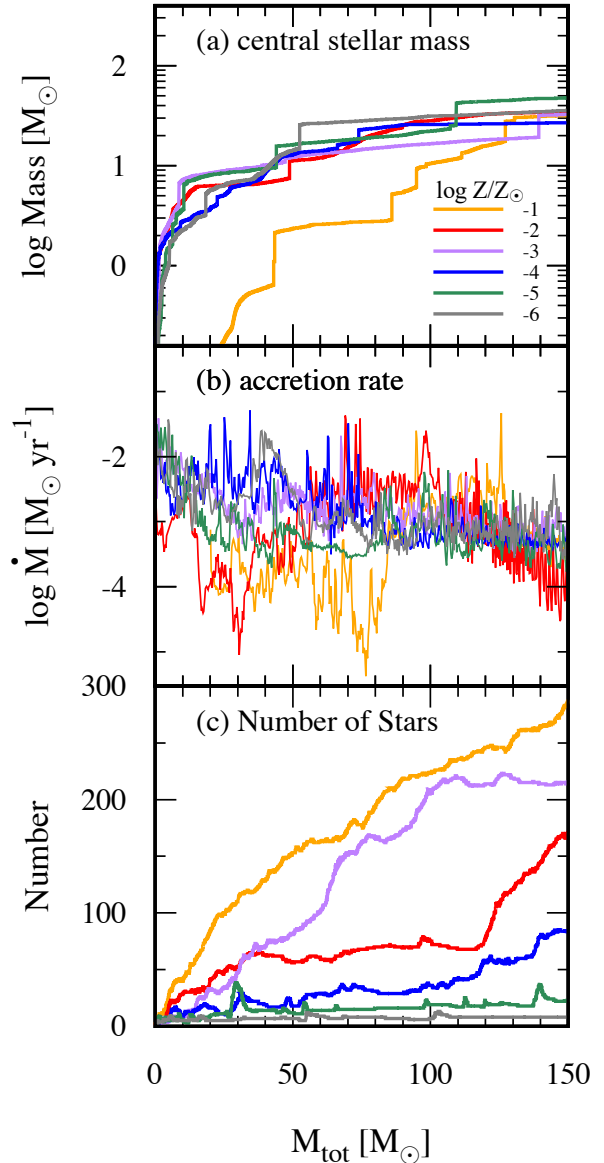


Figure 7. Evolution of (a) the mass of the central stars, (b) the mass accretion rate onto the central stars, and (c) the number of the stars formed in the cloud as a function of the total stellar mass M_{tot} for $\log Z/Z_{\odot} = -1$ (yellow), -2 (red), -3 (purple), -4 (blue), -5 (green), and -6 (grey). Since M_{tot} increases with time (Fig. 6), the horizontal axis represents a time sequence from left to right. Here, we define the central star as the most massive star at $M_{\text{tot}} = 150 M_{\odot}$.

small fragments as shown in the $Z/Z_{\odot} = 10^{-4}$ case since dust cooling becomes efficient only when $n \gtrsim 10^{11} \text{ cm}^{-3}$.

In the models with $Z/Z_{\odot} = 10^{-3}$ and 10^{-2} , the circumstellar disk becomes strongly unstable and widespread fragmentation leads to the formation of a large number of protostars. This instability is mainly caused by dust cooling, which significantly reduces the gas temperature at $n \gtrsim 10^8 \text{ cm}^{-3}$. Such dust-induced fragmentation leads to the formation of low-mass stars with typical masses of $0.01\text{--}0.1 M_{\odot}$, reflecting the Jeans mass of the adiabatic cores (e.g. Omukai et al. 2005; Chon & Omukai 2020). Many of them show negligible

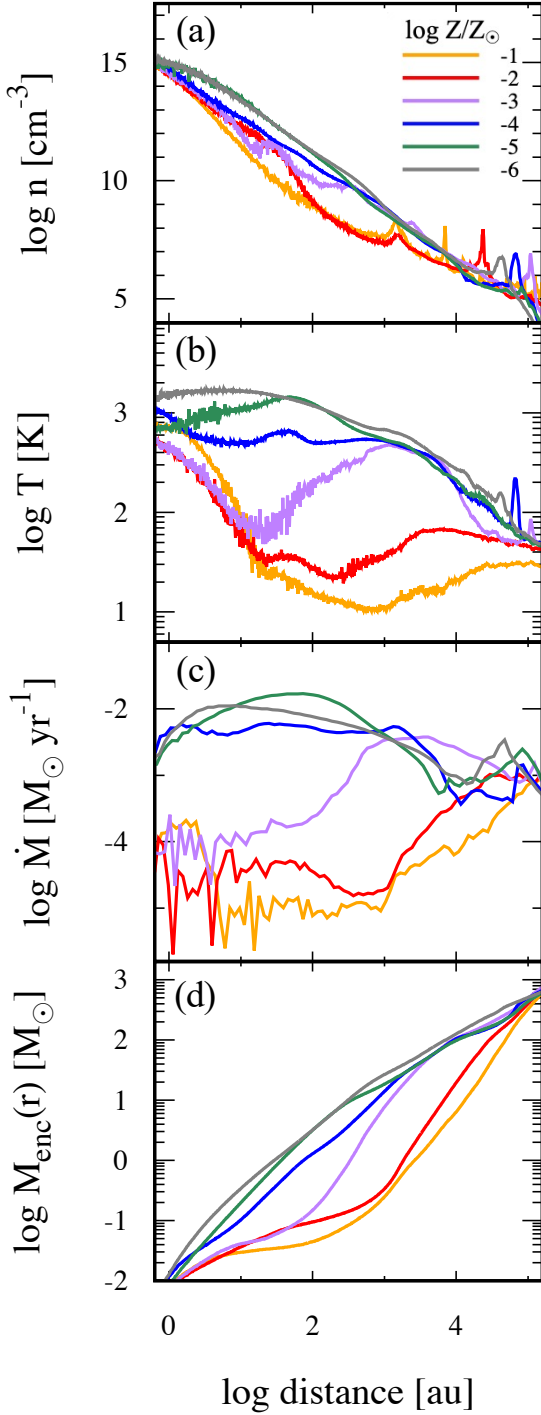


Figure 8. Radial profiles of (a) the density, (b) the temperature, (c) the inflow rate, and (d) the enclosed mass inside the given radius at the moment when the star is formed. Different colors show the profiles with $\log Z/Z_{\odot} = -1$ (yellow), -2 (red), -3 (purple), -4 (blue), -5 (green), and -6 (grey).

increase in mass, as they are ejected from the disk soon after their birth due to gravitational interaction with the central massive stars and with the spiral arms. Once ejected, they wander in the low-density outskirts and the mass growth almost ceases in such cases. When $Z/Z_{\odot} = 10^{-1}$, the circumstellar disk forms but its size is much smaller than those found at lower metallicities. In this case, since strong turbulence survives until the later accretion stage, rotational motion is subdominant compared to the turbulent motion. Due to the turbulent random motion, the angular momentum of the accreting gas does not align in the same orientation, and the disk structure is hard to form. The number of fragments formed in the disk is much smaller than in the lower metallicity cases. Instead, fragmentation mainly takes place along the filament, rather than in the circumstellar disk.

Fig. 6 shows the time evolution of the total stellar masses until they reach $150 M_{\odot}$. We can see that the star formation time-scale is the shortest for the intermediate metallicity cases $Z/Z_{\odot} \sim 10^{-4} - 10^{-3}$. In such cases, rapid cooling in the high-density regime $n \sim 10^{10} \text{ cm}^{-3}$ accelerates cloud collapse and induces vigorous star formation, making the star formation time-scale very short. In lower metallicity cases, inefficient cooling results in higher temperature and thus higher pressure support, which delays the cloud collapse and star formation. On the other hand, in higher metallicity cases, the star formation time-scale increases again with increasing metallicity. In this case, star formation is locally accelerated by the efficient cooling and compression by the turbulent motion. This allows the first protostar to form earlier at higher metallicity: the onset of star formation is $\sim 1t_{\text{ff}}$ for $Z/Z_{\odot} = 0.01-0.1$, while ~ 1.7 and $3t_{\text{ff}}$ for $Z/Z_{\odot} = 10^{-3}$ and 10^{-4} , respectively. In the $Z/Z_{\odot} = 0.01-0.1$ cases, however, the turbulent motion increases the gas density only locally and then only a small amount of gas accumulates around the cloud center at the time of the first protostar formation (see also Fig. 8d). This implies that a longer interval of time is required for accumulation of a gas reservoir and subsequent episode of star formation in $0.1-0.01 Z_{\odot}$ with respect to the intermediate metallicity cases.

Fig. 7 (a) and (b) show the evolution of the mass and the mass accretion rate for the most massive protostar at the end of our simulation, respectively. The horizontal axis represents the total stellar mass in our simulated region and can be interpreted as a time sequence going from left to right. We can see that the mass growth histories of the central stars are similar among the different metallicity cases with the exception of the highest metallicity model. The typical accretion rates at the end of the simulation converge to $\sim 10^{-3} M_{\odot} \text{yr}^{-1}$, while the rates for $Z/Z_{\odot} \gtrsim 10^{-2}$ are initially smaller by an order of magnitude compared to the lower metallicity cases. The similarity in the late time evolution comes from the fact that the most massive protostars are located at the center of the cloud. The gas accumulates onto the cloud center, attracted by the sum of the gravity of the gas and stars in the system. On the other hand, in the case of $Z/Z_{\odot} = 0.1$, the sites of protostar formation is more controlled by persistent turbulent motions rather than the overall gravity of the cloud, and do not cluster around the cloud center. This results in the difference in the later time accretion history.

Fig. 7(c) shows the number of protostars as a function of the total stellar mass. There is a trend that the number of stars increases with increasing metallicity, since efficient cool-

ing induces the formation of a large number of fragments. Between the models with $Z/Z_{\odot} = 10^{-3}$ and 10^{-2} , however, this trend is reversed: a larger number of stars form when $Z/Z_{\odot} = 10^{-3}$ compared to the $Z/Z_{\odot} = 10^{-2}$ case. This is because the temperature at $n \sim 10^8 \text{ cm}^{-3}$ is much higher in $Z/Z_{\odot} = 10^{-3}$ than in the 10^{-2} model, which makes the Jeans mass accordingly higher.

Fig. 8 quantitatively explains why the number of protostars is larger when $Z/Z_{\odot} = 10^{-3}$ than in the $Z/Z_{\odot} = 10^{-2}$ model, showing the radial profiles of the density (panel a), temperature (b), inflow rate (c), and enclosed mass inside the radius r (d) as a function of the distance from the cloud center r when the first protostar forms. Here, we evaluate the radial profiles of the inflow rate by $4\pi r^2 \rho v_{\text{inf}}$ where v_{inf} is the infall velocity toward the protostar, averaged over the gas at the distance r . The temperature profiles are quite different among the different metallicities. At $r \lesssim 10^4 \text{ au}$, the temperature is much lower in the high metallicity cases with $Z/Z_{\odot} \gtrsim 10^{-2}$ than in the low metallicity cases with $Z/Z_{\odot} \lesssim 10^{-4}$ due to efficient cooling at densities with $n \sim 10^6 \text{ cm}^{-3}$. This makes the accretion rate, which is proportional to $T^{3/2}$ (Larson 1969; Shu 1977), much higher in the lower metallicity cases at this scales. The case with metallicity $10^{-3} Z_{\odot}$ is transitional in the sense that the temperature profile is close to that of the higher metallicity in the inner region with $r \lesssim 10^2 \text{ au}$ but close to that of the lower metallicity in the outer region with $r \gtrsim 10^3 \text{ au}$. This causes a decrease in the inflow rate inward, from $10^{-3} M_{\odot} \text{ yr}^{-1}$ in the outer region to 10^{-4} inside. The gas accumulates at around 10^3 au and the circumstellar disk becomes highly unstable, leading to the formation of a larger number of protostars in this case (Tanaka & Omukai 2014).

Our results qualitatively agree with those obtained by Tanaka & Omukai (2014), where the circumstellar disk becomes gravitationally unstable when $Z/Z_{\odot} \sim 10^{-4} - 10^{-3}$, although with the following quantitative difference: the disk is most unstable at $Z/Z_{\odot} = 10^{-4}$ in their analysis, while in our case it is more unstable at $Z/Z_{\odot} = 10^{-3}$ and 10^{-2} . This is caused by the different mass accretion rate from the cloud envelope onto the circumstellar disk. The actual mass accretion rate in our simulation is $10^{-3} - 10^{-2} M_{\odot} \text{ yr}^{-1}$ in the metallicity range $Z/Z_{\odot} \lesssim 10^{-2}$ (Fig. 8 c), higher than assumed by Tanaka & Omukai (2014), where $c_s^3/G \simeq 10^{-4} M_{\odot} \text{ yr}^{-1}$ at $Z/Z_{\odot} \gtrsim 10^{-3}$. This larger accretion rate leads to a more unstable circumstellar disk at $Z/Z_{\odot} = 10^{-2}$ and 10^{-3} , yielding a large number of low-mass stars in our study.

Fig. 9 presents the time evolution of the number of stars found in our calculation. Also shown by the dashed line is the relation in the case of the primordial star formation, which is proposed by Susa (2019), who compiled his own long-term simulation results and those by other authors:

$$N(t) = 3 \left(\frac{t_{\text{ff,ad}}}{t_{\text{ff,th}}} \frac{t}{1 \text{ yr}} \right)^{0.3} \equiv 3 \left(\frac{\tilde{t}}{1 \text{ yr}} \right)^{0.3}, \quad (5)$$

where t is the elapsed time since the first protostar is formed, $t_{\text{ff,ad}}$ is the free-fall time at $n_{\text{ad}} = 10^{19} \text{ cm}^{-3}$, and $t_{\text{ff,th}}$ is the free-fall time at the density, where the sink particle is introduced. When $Z/Z_{\odot} = 10^{-6}$ (grey), the number of stars is at the lower-edge of the shaded region. When $Z/Z_{\odot} = 10^{-4}$ (green) and 10^{-5} (blue), the number roughly follows eq. (5). In those cases, the stellar number sometimes decreases due to stellar mergers while it increases by disk fragmentation afterward. Although this causes fluctuations in the number of

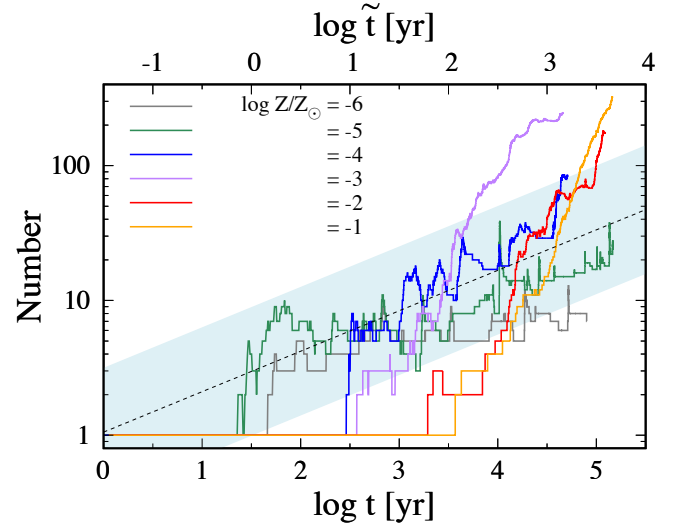


Figure 9. Time evolution of the stellar number for the metallicity with $\log Z/Z_{\odot} = -1$ (yellow), -2 (red), -3 (purple), -4 (blue), -5 (green), and -6 (grey). The black dashed line show the fitting formula (eq. 5), proposed by Susa (2019). We overplot the blue shaded region, which is scatter of the stellar numbers found in the studies on the primordial star formation. The upper horizontal axis shows the scaled time \tilde{t} , which is defined in eq. (5).

stars, its time average roughly obeys the relation of eq. (5). Note that the decrease due to the mergers in this metallicity range is also reported by Shima & Hosokawa (2021), whose study follows the evolution in a few thousand years. Our result suggests that the number of stars increases in a later stage than calculated in their study and behaves similarly to the primordial case. Above $Z/Z_{\odot} = 10^{-3}$, the number of stars increases more steeply than in the lower metallicity cases and no longer obeys eq. (5). In those cases, the circumstellar disk is highly unstable due to the dust cooling and a number of stars are ejected by the close stellar encounters (see Fig. 5). In addition, fragmentation of the filament at larger scales ($10^4 - 10^5 \text{ au}$) further boosts the number of stars in the case of $Z/Z_{\odot} \gtrsim 10^{-2}$. Such effects as the stellar ejection and the fragmentation of the filament at the larger scale cause the deviation of the number of stars from eq. (5) at $Z/Z_{\odot} \gtrsim 10^{-3}$.

Note that the thermal evolution in our study is different from that in Susa (2019), even for the case with $Z/Z_{\odot} = 10^{-6}$. In our simulation, HD cooling becomes important and the temperature becomes smaller than 100 K at low density regions with $n \lesssim 10^8 \text{ cm}^{-3}$ (see Fig. 3). This causes smaller gas infall rate toward the cloud center (e.g. Hirano et al. 2015) compared to the case where the HD cooling does not effective. As a result, the circumstellar disk becomes smaller in mass and more stable against gravitational instability, leading to a smaller number of stars. In fact, the number evolution in $Z/Z_{\odot} = 10^{-6}$ (grey line) lies slightly outside the shaded region.

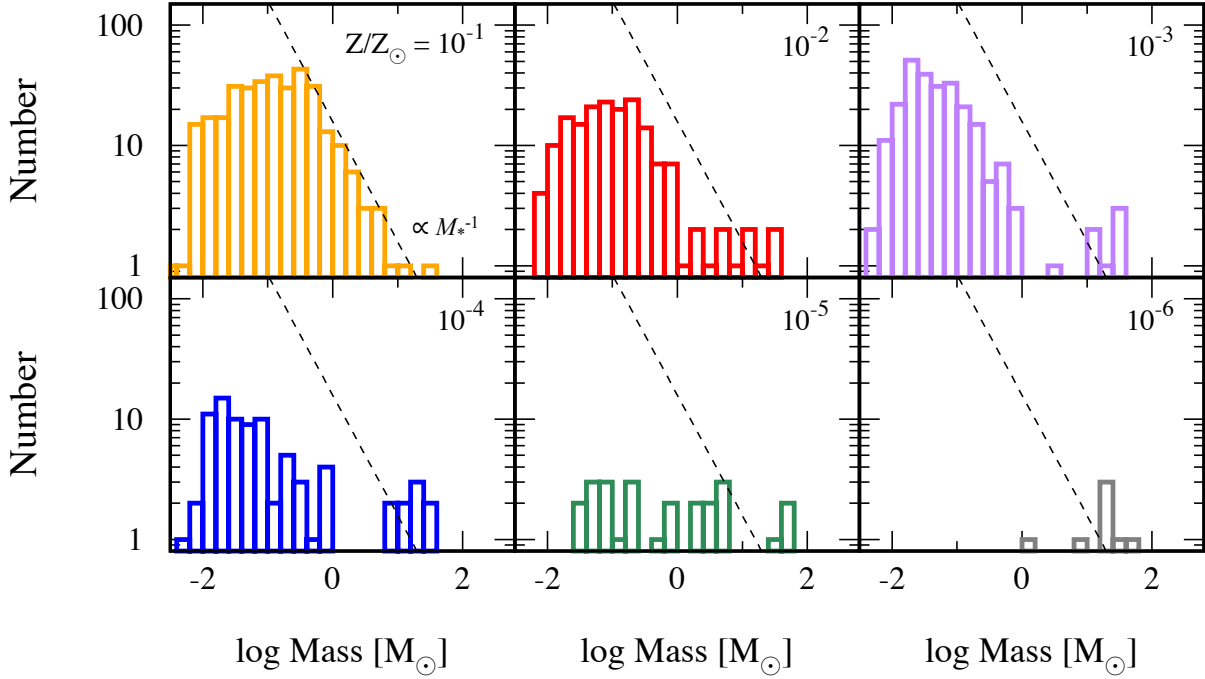


Figure 10. The mass distribution when the total stellar mass reaches $150 M_{\odot}$ for the different metallicity models. The vertical axis represents the number of stars in each mass bin. The black dashed lines show $dN/d \log M_* \propto -1$, where N is the number density in each mass bin, which has an equal width in logarithm.

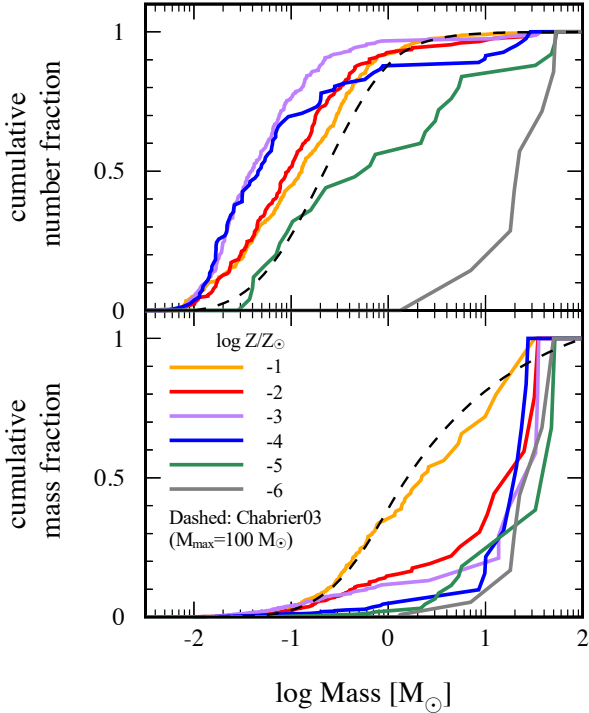


Figure 11. Cumulative number (top) and mass fraction (bottom) for $\log Z/Z_{\odot} = -1$ (yellow), -2 (red), -3 (purple), -4 (blue), -5 (green), and -6 (grey). Black dashed lines represent the cumulative distributions when we assume a Chabrier IMF (Chabrier 2003) with the maximum stellar mass of $100 M_{\odot}$.

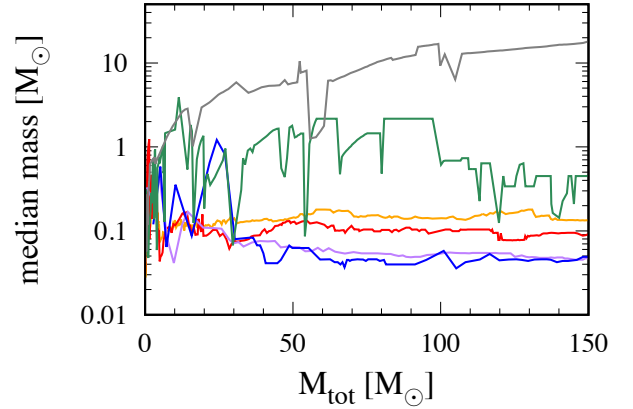


Figure 12. Evolution of the median mass as a function of the total stellar mass for $\log Z/Z_{\odot} = -1$ (yellow), -2 (red), -3 (purple), -4 (blue), -5 (green), and -6 (grey).

3.3 Mass function of the protostars

Fig. 10 shows the mass distribution of the protostars for the different metallicities when the total stellar mass reaches $150 M_{\odot}$. We can see that the distribution gradually shifts from top-heavy to Salpeter-like with increasing metallicity. For example, when $Z/Z_{\odot} = 10^{-6}$, all the protostars have masses larger than $1 M_{\odot}$ and the typical mass is several tens of solar mass. When $Z/Z_{\odot} = 10^{-5}$, the mass distribution becomes log-flat with the minimum stellar mass of $0.01 M_{\odot}$. When $Z/Z_{\odot} \gtrsim 10^{-4}$, a larger number of low-mass stars are

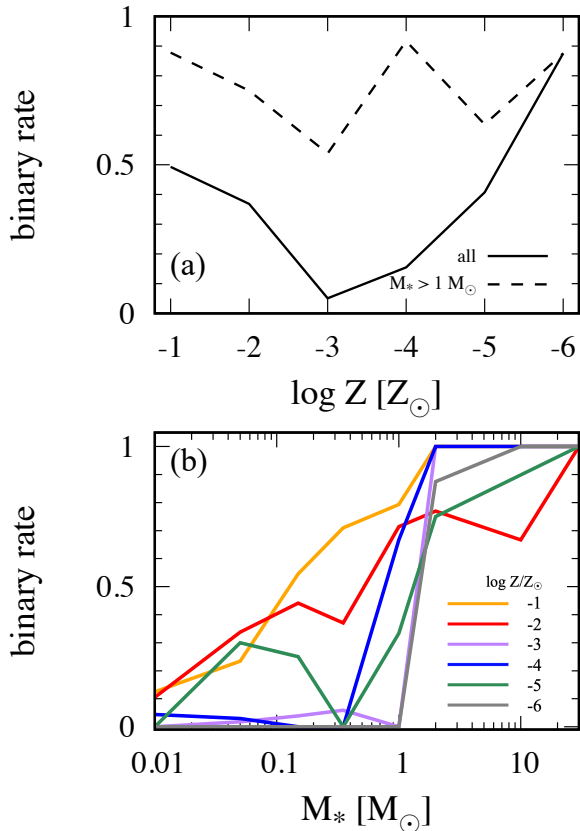


Figure 13. (a) Fraction that stars belong to a binary or multiple system for all the stars (solid) and massive stars with $M_* > 1 M_\odot$ (dashed) as a function of metallicity when the total stellar mass reaches $150 M_\odot$. (b) Fraction of stars belonging to a binary or multiple system as a function of metallicity for $\log Z/Z_\odot = -1$ (yellow), -2 (red), -3 (purple), -4 (blue), -5 (green), and -6 (grey).

formed due to dust-induced fragmentation. This trend is consistent with the results of simulations by Dopcke et al. (2011, 2013), where the number of low-mass stars increases with increasing metallicity. The mass distribution for such low-mass stars is universal across a wide range of metallicity values: the number peaks at $0.01\text{--}0.1 M_\odot$ and declines in proportion to M_*^{-1} at the massive end. This universal distribution is consistent with those found in previous studies (Bate 2009; Safraneck-Shrader et al. 2014, 2016; Bate 2019). In addition to this universal profile, we can find a massive stellar component in the mass range of $1\text{--}50 M_\odot$ when $Z/Z_\odot \lesssim 10^{-2}$. The number of stars associated with this component exceeds that expected from a simple extrapolation from the lower mass end with the scaling M_*^{-1} .

To quantitatively compare the mass function for the different metallicities, we plot in Fig. 11 the cumulative number (panel a) and mass distribution (b) normalized by the total stellar number and mass, respectively. The dashed line shows the cumulative fraction assuming the Chabrier IMF with the maximum mass of $100 M_\odot$ (Chabrier 2003). The cumulative number fraction for $Z/Z_\odot \gtrsim 10^{-4}$ indicates that the number of stars is dominated by low-mass stars with $M_* \lesssim 1 M_\odot$. This is consistent with the results obtained by previous stud-

ies, where the dust cooling induces the formation of a number of small stars (Clark et al. 2008; Dopcke et al. 2011, 2013; Safraneck-Shrader et al. 2016). In terms of number fraction, the critical metallicity is $Z_{\text{crit}} \sim 10^{-5} Z_\odot$, above which low-mass stars with $M_* < 1 M_\odot$ dominate the total number.

On the other hand, the cumulative mass fraction indicates that the mass fraction of low-mass stars is below 10% in $Z/Z_\odot \lesssim 10^{-2}$ cases. This value is much smaller than that expected from the Chabrier IMF (40%), indicating that the mass function is still top-heavy at these metallicities. This means that the massive stars at the cloud center efficiently accretes mass, while dust cooling produces a large number of small fragments. When $Z/Z_\odot = 10^{-1}$, the cumulative mass fraction becomes very close to the Chabrier IMF. Therefore, in terms of the mass fraction, the critical metallicity is $Z_{\text{crit}}/Z_\odot \sim 10^{-2} - 10^{-1}$, below which the mass function becomes top-heavy compared to the present-day IMF.

Fig. 12 plots the time evolution of the median mass as a function of the total stellar mass, showing that it almost converges to $\sim 0.1 M_\odot$ for $Z/Z_\odot \gtrsim 10^{-4}$. Since the number of stars is dominated by the low-mass component, this indicates that the stellar mass distribution of the low-mass stars does not evolve with time: existing stars increase their mass by gas accretion, while new low-mass stars continue to form, which makes the overall shape of the stellar mass distribution unchanged over time (e.g. Bate et al. 2003). This supports our interpretation of the mass distribution found by the simulations as the IMF. Still radiative feedback from the stars can affect the gas distribution and mass growth rate, as will be discussed in Sec 4.2.

3.4 Statistical properties of stellar binaries and multiple systems

In our simulation, some stars are formed as binary or multiple stellar systems with other stars. Statistical properties of the binaries are important in comparing our results with observations to verify our models. Recent gravitational wave detection have shown the existence of merging BHs with component mass larger than $30 M_\odot$ (e.g. Abbott et al. 2016, 2021). Several authors insisted that such massive BHs are likely to be the end product of metal-poor or metal-free stars, where reduced mass loss rate allows massive BHs to form (e.g. Belczynski et al. 2010; Kinugawa et al. 2014; Schneider et al. 2017; Marassi et al. 2019; Spera et al. 2019; Graziani et al. 2020). Here, we discuss how the initial metallicity alters the stellar binary properties.

We define a pair of two stars to form a binary system if the total energy E_{tot} is negative:

$$E_{\text{tot}} = \frac{M_1 v_1^2}{2} + \frac{M_2 v_2^2}{2} - \frac{GM_1 M_2}{r_{\text{sep}}} < 0, \quad (6)$$

where M_1 and M_2 are the masses of the pair of stars, v_1 and v_2 are the velocities of the two stars relative to that of the center of mass, and r_{sep} is the separation of the stars. In our simulation, stars often form a gravitationally bound group composed of more than two members, so-called a higher-order multiple system. Following Bate et al. (2003), we identify the hierarchically bound stellar groups according to the following procedure: once we find a binary, we substitute the binary pair by a single stellar component, whose position and velocity are those of the center of the mass of the binary. We then

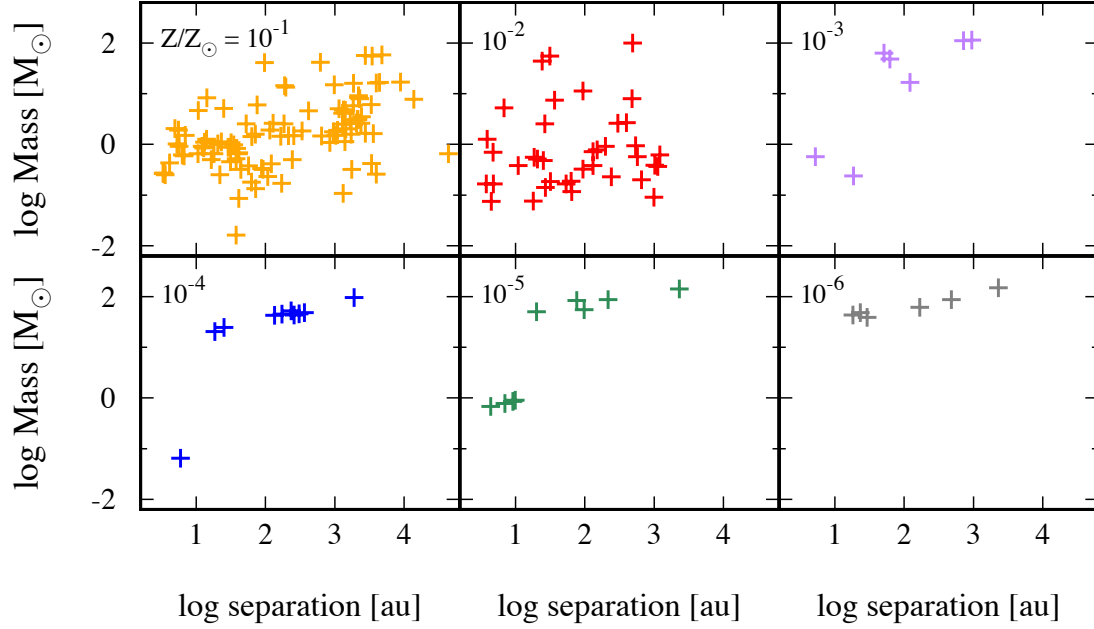


Figure 14. Total mass versus separation of binary systems for different metallicity models when the total stellar mass reaches $150 M_{\odot}$.

find the bound pairs with this substituted component and if it forms a binary with another star, we again substitute it with a single component. By repeating the above process, we recurrently identify higher-order multiple systems.

In Fig. 13(a), the solid (dashed) line shows the probabilities that a star (a star with the mass larger than $1 M_{\odot}$, respectively) belongs to a binary system. The binary rate decreases with decreasing metallicity when $Z/Z_{\odot} \gtrsim 10^{-3}$. This trend can be interpreted as a consequence of the cloud morphology. When $Z/Z_{\odot} = 10^{-3}$, the cloud collapses monolithically toward the cloud center, and a number of stars are packed in the compact central region. In such a situation, close stellar encounter frequently occurs, which ejects stars from the system or breaks the bound binary pairs, reducing the binary rate in the lower-metallicity cases. In contrast, when $Z/Z_{\odot} = 10^{-1}$, the filamentary structure develops and stars form across a wide range in the cloud scales and close stellar encounter is relatively rare compared to the lower-metallicity cases. This environment is favorable for the formed binaries to avoid destruction by the stellar encounters, and the binary rate becomes higher than in the lower metallicity cases.

The binary rate of the stars with $M_* > 1 M_{\odot}$ seems to have little correlation with the cloud metallicity especially when $Z/Z_{\odot} \lesssim 10^{-4}$, since it is mainly determined by the stochastic interaction between the massive stars at the cloud center. Some massive stars are ejected from the cloud center via multi-body interaction, which reduces the binary rate at $Z/Z_{\odot} = 10^{-5}$. Our result indicates that such massive stars residing at the cloud center usually form binary or multiple systems, which is often observed in primordial star formation (e.g. Stacy et al. 2016; Chon et al. 2018; Susa 2019). On the other hand, the binary rate of all the stars strongly depends on the metallicity. This is because the number of low mass stars becomes larger for higher metallicity as dust cooling in-

duces vigorous fragmentation. Since low mass stars are easily ejected from the cloud and have smaller chance to form binary with other stars, the binary rate becomes smaller at $Z/Z_{\odot} = 10^{-3}$ than in lower metallicity environments.

Fig. 13(b) shows the binary rate as a function of the stellar mass. Stars more massive than $2 M_{\odot}$ are mostly found in the binary system with its fraction somewhat depending on the metallicity. Below $2 M_{\odot}$, the binary rate becomes small due to the stellar ejection by the close stellar encounter, in which low-mass stars are more easily ejected than massive stars. Once ejected, stars have little chance to make binaries with other stars, which significantly reduces the binary rate of the ejected low-mass stars. When $Z/Z_{\odot} \lesssim 10^{-3}$, this decrease is rather dramatic. In this case, since formed stars are closely packed in the central compact region, the stellar encounter and the ejection happen more frequently. As a result, most of the low-mass stars are ejected and the binary rate falls sharply at $M_* \lesssim 1 M_{\odot}$. On the other hand, when $Z/Z_{\odot} \gtrsim 10^{-2}$, the decrease of the binary rate is more gradual. In this case, formed stars are spatially distributed over the entire cloud core since stars are formed not only by the disk fragmentation but also by the filament fragmentation (see Fig. 5). Owing to less frequent stellar encounter, low-mass stars formed in less dense region have more chance to make binaries before the ejection. Note that stars formed inside the disk, i.e., dense region, are ejected and hardly end up in binaries also in this case.

Fig. 14 shows the total mass and separation of the binaries for different metallicities. When $Z/Z_{\odot} \lesssim 10^{-3}$, it is hard to find a typical separation for the binaries. In these cases, massive stars form hierarchical binaries (bottom panel of Fig. 5). The separation of the closest binaries in those hierarchical systems is ~ 10 au. Those tight binaries are embedded in hierarchical systems with one or two companion(s) at separa-

ration of a few 100 au, forming triple or quadratic systems. They also belong to higher-order multiple systems, with separation of a few 1000 au. Such hierarchical systems are often observed in simulations of primordial (Susa 2019) or present-day star formation (e.g. Bate 2009, 2019). A small number of low-mass binaries with mass of $0.1 - 1 M_{\odot}$ are also found, whose separation is smaller than 10 au. We find that those low-mass binaries have been ejected from the cloud center due to the close encounter with massive stars, which terminated the further mass growth. Such ejected low-mass binaries tend to have small separations, otherwise the binary is destroyed during the close encounter with massive stars. When $Z/Z_{\odot} = 10^{-2}$, a massive hierarchical system resides at the cloud center surrounded by a large number of low-mass stars (see the bottom panel of 5). This system is composed of two tight binaries with separation of a few 10 au, forming a massive quadruple system as in the cases with lower metallicity. Low-mass binaries have separation of a few $- 10^3$ au, which is not observed in the lower metallicity cases. When $Z/Z_{\odot} = 10^{-1}$, a large number of low-mass tight binaries appear while massive binaries typically have larger separations.

We have also seen that tight binary systems form in hierarchical multiple systems. Previous studies have shown that the separation of an isolated binary system increases as it acquires the angular momentum from the accreted matter (Susa 2019; Chon & Hosokawa 2019). In contrast, if a binary is embedded in a hierarchical system, the outer-most object preferentially acquires the angular momentum and increases its separation with the inner objects, while the separation of more inner systems does not grow over the simulated period as long as they do not experience a close encounter with another star. This fact is consistent with previous studies on the primordial star formation, in which the authors observed the formation of massive binary systems (e.g. Stacy et al. 2016; Sugimura et al. 2020).

Our results show that the formation of the massive tight binaries is expected for all the metallicity range considered here. Their separations are typically ~ 10 au and show little evolution with time. This supports the idea that merging BH binaries are formed in low-metallicity environments, including the primordial case. Still the separation is too large for the binary to coalesce within the Hubble time via the GW emission, if it evolves into a BH binary (Peters 1964). Since the minimum binary separation set by the numerical resolution is \sim au, binaries with sub-au separation cannot be resolved in our calculation. Since higher-order multiple systems are observed down to 10 au scales, multiple systems with even smaller separation could be found in calculations with higher spatial resolution of sub-au scale. To investigate the possibility whether low-metallicity clouds yield merging binary BHs, we need to further resolve the stellar radii and follow binary formation at sub-au separations.

4 DISCUSSION

4.1 Transition from top-heavy to present-day IMF

We have studied the impact of metallicity on the stellar mass spectrum and found that the number of low-mass stars ($M_{*} < 1 M_{\odot}$) increases with metallicity. Our results are not only consistent with previous studies on the mass functions found in low-metallicity environments (Clark et al.

2008; Dopcke et al. 2011, 2013; Safronek-Shrader et al. 2016), but also exemplifies a natural transition to the present-day Salpeter-like IMF found by numerical studies of stellar cluster formation in the literature (Bate et al. 2003; Bonnell et al. 2006; Bate 2009; Krumholz et al. 2012; Bate 2019). Here, we briefly compare our findings with previous results and discuss how the metallicity effect modifies the stellar mass spectrum.

Previous numerical studies have shown that in low-metallicity environments with $Z/Z_{\odot} \lesssim 10^{-4}$ the existence of a trace amount of metals leads to the formation of low-mass stars owing to fragmentation induced by dust cooling (Clark et al. 2008; Dopcke et al. 2011, 2013; Safronek-Shrader et al. 2016). For example, Dopcke et al. (2013) have found that the stellar mass distribution is log-flat for $Z/Z_{\odot} \lesssim 10^{-5}$, while the Salpeter-like power law distribution with the peak mass of $0.1 M_{\odot}$ develops when $Z/Z_{\odot} = 10^{-4}$. Still, their calculations are extended only up to several hundred years and most of massive protostars are still vigorously accreting the mass at the end of the simulation, so the mass distribution can still change with time. Our results are consistent with their findings for this metallicity range, if we focus on the mass distribution at the low-mass end, i.e., log-flat for $Z/Z_{\odot} \lesssim 10^{-5}$ while Salpeter-like for $Z/Z_{\odot} \gtrsim 10^{-4}$.

One big difference between our and previous results can be observed at the high-mass end of the mass distribution, i.e., the existence of massive stars with several $10 M_{\odot}$. This massive component cannot be accounted for by a simple extrapolation from the Salpeter-like power-law tail developed at the lower masses. This is a natural consequence of the fact that the stellar mass at the high-mass end is mainly determined by the cluster’s gravitational potential. The massive protostars preferentially grow in mass, since they reside at the bottom of the gravitational potential well, as typically quoted in the “competitive accretion” model (Bonnell et al. 2006). Their masses are almost independent of the gas metallicity, which only alters the thermal state of the cloud and thus the typical mass of the fragments (e.g. Larson 2005).

When the metallicity is $Z/Z_{\odot} = 0.1$, a highly filamentary structure develops, which is often seen in the present-day stellar cluster formation in a turbulent cloud core (Li et al. 2003; Bate et al. 2003; Bonnell et al. 2004; Jappsen et al. 2005; Smith et al. 2011; Krumholz et al. 2012; Guszejnov et al. 2018). This is also consistent with the morphology of the observed star forming regions by Herschel space observatory (e.g. André et al. 2010; Könyves et al. 2015; Marsh et al. 2016). We have shown that dust cooling at $n \gtrsim 10^6 \text{ cm}^{-3}$ lowers the effective ratio of specific heat γ below unity and causes the growth of the filamentary mode of the gravitational instability (e.g. Bastien 1983; Inutsuka & Miyama 1992; Hanawa & Matsumoto 2000; Tsuribe & Omukai 2006). Our results suggest that such a filamentary structure does not develop for $Z/Z_{\odot} \lesssim 10^{-3}$, since the cooling rate in shock compressed gas is small and boosted pressure support prohibits the growth of the filamentary mode. This value of the critical metallicity is consistent with several observational evidences. For example, the fraction of carbon-enhanced stars increases with decreasing metallicities, which can be explained by the IMF transition at $Z_{\text{crit}}/Z_{\odot} \sim 10^{-2.5}$ (Suda et al. 2013; Lee et al. 2014). To reproduce the observed profiles of globular clusters, Marks et al. (2012) suggests that the top-heavy IMF is realized in low-metallicity environment with $Z/Z_{\odot} \sim 10^{-2}$ to 10^{-1} . They explain the trend that the lower-metallicity clus-

ters have lower concentration of low-mass stars by considering the top-heavy IMF, which quickly depletes the cluster gas.

We claim here that monolithic collapse of the central massive core leads to formation of central massive stars, and thus to a top-heavy IMF. Once the turbulent motion decays, the filamentary structure no longer develops as seen in the $Z/Z_{\odot} \lesssim 10^{-3}$ case. In this case, the gas accumulates at the cloud center, forming a massive circumstellar disk. Since a large amount of mass is confined to the small central region, massive stars in this region can efficiently accrete mass. Dust cooling induces vigorous fragmentation inside the disk and produces a number of low-mass stars, while they are easily ejected from the system as they experience many-body interactions with other stars (Clark et al. 2008; Dopcke et al. 2013; Safraneck-Shrader et al. 2016; Chon & Omukai 2020) or migrate inward due to the interaction with the disk gas and merge with the central stars (e.g. Tanaka et al. 2002; Chon & Hosokawa 2019). This makes the massive stars more massive, producing a high-mass stellar component distinctive from the distribution of the low-mass stellar component.

Survival of the turbulent motion is the key to form a filamentary structure (e.g. Krumholz et al. 2012). In our study, we impulsively inject a turbulent energy at the initial collapse stage, which decays over the time-scale of the sound crossing time or the free-fall time of the cloud (e.g. Stone et al. 1998; Mac Low 1999; Bate et al. 2003). The turbulence can be continuously driven by the external forcing, such as the expansion of the H II region or injection of mechanical energy by SN explosions outside our simulation box. How such forcing works in low-metallicity environments is still unclear. Nonetheless, we expect inefficient cooling in the low-metallicity gas to strongly resist turbulent compression and to suppress the formation of filamentary structure even when the turbulent energy is continuously injected. Such continuous forcing in low-metallicity environments would delay the cloud collapse and can lead to formation of more massive stars compared to non-turbulent clouds (e.g. McKee & Tan 2003).

Our results can also have strong impact on the chemical evolution of galaxies. Larson (1998) discussed the possibility that a top-heavy IMF in the early universe causes rapid chemical enrichment and thereby reduces the number of low-metallicity stars. This can be a clue to the so-called classical ‘G-dwarf problem’ (Tinsley 1980), i.e., the number of low-metallicity stars are smaller than theoretical expectation in the closed-box model without gas inflow or outflow (Salvadori et al. 2007). Larson (1998) also suggested that a top-heavy IMF in the early universe can explain a large amount of heavy elements observed in hot gas of galaxy clusters. Effect of a metallicity-dependent IMF on the chemical evolution of galaxies has been studied by some authors. de Bressana et al. (2017) showed that a top-heavy IMF in primordial minihalos successfully reproduces the metallicity distribution of the low-metallicity stars in the Galactic halo. Other studies on Galactic chemical evolution showed that a top-heavy IMF in low-metallicity environments solves the G-dwarf problem but fails to reproduce the observed abundance patterns (Chiappini et al. 2000; Martinelli & Matteucci 2000; Ballero et al. 2006). The IMFs assumed in their studies, i.e., single power-law simple IMFs, however, are different from our finding, i.e., Salpeter-like IMFs plus massive components with several $10M_{\odot}$ in low-metallicity environments. Effects of the

IMF derived in this paper on galaxy formation and evolution is worth examining quantitatively in future studies.

4.2 The impact of radiative feedback and magnetic field on IMF

Protostars are still accreting the gas at the end of our simulation since we do not include any feedback effects from the forming stars, which can halt further mass accretion. The ionizing radiation emitted from massive stars is one of the leading processes that disperse the surrounding gas and terminates mass accretion (Peters et al. 2010; Dale et al. 2012; Walch et al. 2012; Geen et al. 2018; He et al. 2019; Fukushima et al. 2020b). He et al. (2019) conducted radiation hydrodynamics simulations and found that while the ionizing radiation decelerates the protostellar mass growth, the functional form of the mass distribution, such as typical stellar mass, slope of the high mass tail, shows little time evolution during their simulation. They provided the following analytical fit to the total star formation efficiency f_* ,

$$f_* = 0.02 \left(\frac{M_{\text{cloud}}}{10^4 M_{\odot}} \right)^{0.4} \left(1 + \frac{\bar{n}}{10^3 \text{ cm}^{-3}} \right)^{0.91}, \quad (7)$$

where M_{cloud} and \bar{n} is the mass and mean density of the initial cloud core, respectively. Using our cloud parameters of $M_{\text{cloud}} = 1950 M_{\odot}$ and $\bar{n} = 10^4 \text{ cm}^{-3}$, we obtain the total stellar mass $\sim 170 M_{\odot}$, which is close to the stellar mass at the end of our simulation.

The impact of the ionization feedback becomes stronger with decreasing metallicity, since the less efficient cooling inside the H II region increases the pressure in the ionized gas, which easily evacuates the cloud gas (He et al. 2019; Fukushima et al. 2020b). Our simulation also suggests that difference in the cloud metallicity changes the collapsing cloud morphology, which can result in difference in the feedback efficiency. For example, when $Z \gtrsim 0.01 Z_{\odot}$, massive stars are spatially distributed over the entire cloud core. Meanwhile, when $Z \lesssim 10^{-3} Z_{\odot}$, massive stars are closely packed around the cloud center, which is surrounded by a gas disk (see Fig. 5). High density in the disk can efficiently attenuate UV radiation from the central stars in the disk plane. Since a large amount of mass is still supplied through the disk plane, the stars would continue to grow in mass despite the UV radiation feedback (e.g. McKee & Tan 2008; Hosokawa et al. 2012). Fukushima et al. (2020a) followed the formation of stars starting from a massive collapsing cloud of $10^3 M_{\odot}$. They found that the total mass of stars reach several hundred solar mass when $Z \lesssim 10^{-3} Z_{\odot}$, meaning that the star formation efficiency is about 50%. To further investigate the impact of metallicity on the star formation efficiency in low-metallicity environments, we should follow the propagation of UV radiation resolving down to the circumstellar disks around massive stars.

Heating due to non-ionizing photons is another important process called ‘‘thermal feedback’’, which can alter the protostellar mass distribution. For stars with $M_* \lesssim 10 M_{\odot}$, the stellar luminosity is dominated by the accretion luminosity (Hosokawa & Omukai 2009; Fukushima et al. 2018). This heats up the dust grains and finally increases the gas temperature, prohibiting further fragmentation and thus formation of low-mass stars (Bate 2009; Omukai et al. 2010; Myers et al. 2011; Bate 2012; Krumholz et al. 2012; Bate 2019). Since

thermal feedback does not prevent converging accretion flows from reaching the central massive stars, its main effect is to reduce the number of low-mass stars, increasing the typical protostellar mass. In our simulation, the fractional number of brown dwarfs are larger than that predicted by the Chabrier IMF (Fig. 11a). This over-abundance of brown dwarfs can be potentially mitigated by the inclusion of thermal feedback (Bate 2009; Krumholz et al. 2012).

Magnetic fields can affect the stellar mass distribution by launching outflows and then reducing the mass accretion rate (Machida et al. 2008a; Federrath et al. 2014; Kuruwita et al. 2017; Matsushita et al. 2018). The magnetic force can also prevent gas fragmentation, thereby reducing the number of low-mass stars (Mellon & Li 2008; Machida et al. 2011; Myers et al. 2013). Still, the magnetic-field strength in low-metallicity environments is very unclear. Several magnetic-field generation mechanisms have been advocated, such as the small-scale dynamo (e.g. Schleicher et al. 2010; Schober et al. 2012) or the amplification during the expanding SNe and H II shells (e.g. Koh & Wise 2016), some of which predict that magnetic fields can be created even in primordial environments. Recent simulations follow the formation of a star cluster starting from a magnetized cloud in the present-day environments (Myers et al. 2014; Cunningham et al. 2018). They conclude that the impact of magnetic fields on the IMF is rather small compared to radiative feedback, leading to a small increase in the peak mass by less than a factor of three. Assuming that the magnetic fields are weaker in low-metallicity environments at high redshift due to the limited time for magnetic field amplification, we may expect the fields to play only a subdominant role in shaping the IMF. On the other hand, the field may modify the mass distribution at the high-mass end by making protostellar disk fragmentation inefficient by removing angular momentum and allowing formation of more massive stars at the cloud center (e.g. Machida et al. 2008a; Kuruwita et al. 2017; Sadanari et al. 2021). If so, this would have significant impact on the efficiency of stellar feedback, for example, increasing the frequency of pair instability supernovae.

4.3 Initial conditions for low-metallicity star formation

In this paper, we have initiated our calculation from the same gas profile regardless of the metallicity, i.e., the Bonnor-Ebert sphere with the central density 10^4 cm^{-3} and temperature 200 K. With high enough metals, i.e., $\gtrsim 10^{-2} Z_{\odot}$, the temperature quickly drops by metal-line cooling after the onset of the calculation. As a result, the temperature profiles become very different depending on the initial metallicity. Once the thermal energy is dissipated away, the thermal evolution plays only a subdominant role in shaping the overall structure of the cloud. Instead, the turbulent motion determines the cloud structure and dynamics. Our results demonstrate the importance of turbulence in low-metallicity environments: thermal evolution mostly controls the dynamics at $Z/Z_{\odot} \lesssim 10^{-3}$, while turbulent motion is more important at $Z/Z_{\odot} \gtrsim 10^{-2}$.

In the lowest-metallicity case with $Z/Z_{\odot} = 10^{-6}$, a realistic initial condition would resemble what is found by cosmological simulations for first star formation in a minihalo. In this study, we have adopted a turbulent cloud as the initial

condition for the calculation, where the turbulent energy is slightly ($\lesssim 2$) larger than in typical minihaloes (e.g. Greif et al. 2012). This difference results in smaller number of fragments in our calculation than in previous studies (cf. Fig. 9). Here, the delayed collapse due to turbulent motion allows the gas to cool more by HD, which leads to smaller accretion rate onto the central protostars after their formation, as the accretion rate depends on the prestellar temperature as $\propto T^{3/2}$. Consequently, the circumstellar disks around the protostars are less massive and fragment less frequently, producing a smaller number of stars when turbulent initial conditions are adopted.

Still, appropriate initial conditions for low-metallicity star formation are currently poorly understood. We have little knowledge about the properties of turbulent motions, gas density structures, etc. In the local Universe, star formation is known to take place inside turbulent molecular clouds with density $100 - 10^4 \text{ cm}^{-3}$. Formation process of molecular clouds has been studied in such scenarios as gravitational instability of dense gas in galactic disks (e.g. Hopkins 2012; Dobbs & Baba 2014; Kruijssen 2014) or thermal instability of colliding flows of warm diffuse atomic medium (e.g. Koyama & Inutsuka 2002; Hennebelle et al. 2008; Inoue & Inutsuka 2009; Inutsuka et al. 2015). With this in mind, as the initial condition of our simulation we took a turbulent cloud with turbulent energy comparable to gravitational energy motivated by observations of local molecular clouds (Larson 1981; Heyer & Brunt 2004). Applicability of such initial condition also to low-metallicity environments needs further justification by both future observations and theoretical inspection. Recently, Kalari et al. (2020) observed the star-forming region Magellanic Bridge C with metallicity $\sim 1/5 Z_{\odot}$ by ALMA and identified an associated filamentary structure. Such morphological study on star forming regions will give us some insight on the initial conditions for star formation in low-metallicity environments. Theoretical studies are also required to reveal the formation process of star-forming clouds. For example, clump formation by thermal instability in low-metallicity environments has been studied by Inoue & Omukai (2015).

We have followed the stellar mass evolution until the total stellar mass reaches $\sim 150 M_{\odot}$, at which epoch the radiation feedback will operate (see section 4.2). Although our simulation is extended longer than the previous studies (Clark et al. 2008; Safronek-Shrader et al. 2016; Chiaki & Yoshida 2020; Shima & Hosokawa 2021), the total stellar mass is still small compared to observed star clusters, whose masses range from ~ 100 to $10^5 M_{\odot}$ (e.g. Krumholz et al. 2019). A more massive stellar cluster would be expected to form, if we start from initially a more massive cloud. Marks et al. (2012) suggested that the IMF can be more top-heavy for increasing initial cloud mass or initial density. This explains why massive globular clusters tend to have lower concentration (De Marchi et al. 2007), because a top-heavy IMF dissipates the cluster gas and makes the cluster less concentrated. Our results suggest that even in more massive systems, inefficient cooling dissipates turbulent motion and leads to a top-heavy mass distribution. The critical metallicity which marks the transition from the top-heavy to Salpeter-like IMF can also depend on the initial cloud mass.

4.4 Other important effects

There are several important effects we have not considered in our simulation. One is the warmer CMB in the high- z universe, which sets the minimum dust and gas temperatures to be $2.72(1+z)$ K. This makes the temperature evolution almost isothermal at the CMB temperature when the gas density is $n \lesssim 10^{10} \text{ cm}^{-3}$, and the metallicity has smaller impact on the cloud evolution because the gas cannot cool below the CMB temperature (Smith & Sigurdsson 2007; Jappsen et al. 2009; Meece et al. 2014; Bovino et al. 2014; Safraneck-Shrader et al. 2014). Riaz et al. (2020) investigated how the CMB temperature affects gas fragmentation and thus the stellar mass distribution. They found that higher CMB temperature suppresses fragmentation, resulting in a top-heavy mass distribution. Still the temperature evolution should not be completely isothermal, since the formation heating of hydrogen molecules increases the gas temperature to a few 100 K (Schneider & Omukai 2010). We will pursue this point in a future paper.

In our simulation, we impose several assumptions about the properties of dust grains, i.e. the dust-size distribution (Mathis et al. 1977), the composition of the dust grains (Semenov et al. 2003), and the mass fraction of metals that condensed into dust grains. We have assumed that all of the above properties follow the distributions or values found in the local ISM, which may not be applicable to the grains in the early universe. Very likely, stellar dust sources (Asymptotic Giant branch stars, supernovae, pair-instability supernovae) and grain growth in the ISM provide different dust properties in low-metallicity environments compared to the present-day Universe (Todini & Ferrara 2001; Nozawa et al. 2003; Schneider et al. 2004; Ginolfi et al. 2018). Since the size of the dust grain is smaller for dust produced by SNe, the cooling rate per unit mass is larger (Schneider et al. 2006), while the total amount of dust grains can be one order of magnitude smaller due to destruction by the reverse shock (Schneider et al. 2012). Grain coagulation and grain growth via the depletion of the heavy element in the gas phase onto the grains during the cloud collapse increases the total mass of dust grains and significantly enhances the efficiency of dust cooling (Hirashita & Omukai 2009; Nozawa et al. 2012; Chiaki et al. 2015). Considering all the above processes, Chiaki et al. (2016) have performed three-dimensional simulation and found that when the gas phase metallicity is above $Z/Z_{\odot} = 10^{-5}$, dust cooling changes the thermal evolution and induces fragmentation, which qualitatively agrees with our results assuming the standard-dust properties. How the different dust properties and grain growth affect the long term evolution and the stellar mass distribution is an important question and further studies are needed in the future.

5 SUMMARY

In this paper, we have followed the gravitational collapse of turbulent cloud cores with initial metallicity in the range of $10^{-6} \lesssim Z/Z_{\odot} \lesssim 0.1$ and studied the impact of metallicity on the stellar mass distribution. As noted by previous studies, we have found that the presence of dust grains promotes fragmentation and leads to the formation of low-mass stars with $0.01\text{--}0.1 M_{\odot}$ when the metallicity is larger than

$10^{-5} Z_{\odot}$. There is a trend that the number of low-mass stars increases with metallicity. Aside from the formation of low-mass stars, the mass function is still top-heavy compared to the present-day IMF in the low-metallicity environments with $Z/Z_{\odot} \lesssim 10^{-2}$. In these cases, a massive stellar component appears at the cloud center. These massive stars preferentially accrete the gas and efficiently grow in mass, resulting in the top-heavy mass distribution. The mass distribution approaches the present-day IMF only for $Z/Z_{\odot} \simeq 10^{-1}$ case, suggesting that the critical metallicity for the IMF transition is $Z/Z_{\odot} = 0.01\text{--}0.1$.

Our results indicate that the stellar mass distribution becomes top-heavy when turbulent motion cannot grow due to inefficient cooling in the low-density regime $n \sim 10^6 \text{ cm}^{-3}$. In this case, star formation begins only after the turbulence decays, as found when $Z/Z_{\odot} \lesssim 0.01$. Subsequently, a single massive core monolithically collapses. The central stellar system is formed surrounded by a massive gas disk, which efficiently feeds the central massive star or drives low-mass stars to migrate inward. This makes the mass distribution more top-heavy than the present-day IMF.

When $Z/Z_{\odot} \simeq 10^{-1}$, fine-structure line cooling is efficient at the scales where turbulent motion dominates, leading to the formation of a filamentary structure. If the filament becomes dense enough for gravitational instability to operate, it fragments into protostellar cores. In this case, the size of the circumstellar disks around massive stars is much smaller than in $Z/Z_{\odot} \lesssim 0.01$ cases, since the accreting gas has different orientation of the angular momentum owing to turbulent motion, preventing the formation of a large disk. As a result, the mass supply rate to massive stars becomes smaller than in the monolithic collapse cases.

Our results suggest that the properties of turbulence seeded in the initial cores is crucial for setting the mass distribution. Such turbulence is mainly driven by physical processes in the external environment, i.e. the expansion of H II shells or the injection of a large amount of kinetic energy by SN explosions. How the turbulence properties influence the mass distribution, as well as its interplay between the cooling and heating due to the detailed radiative processes should be further studied.

ACKNOWLEDGEMENTS

This work is financially supported by the Grants-in-Aid for Basic Research by the Ministry of Education, Science and Culture of Japan (SC:19J00324, KO:25287040, 17H01102, 17H02869). RS acknowledges support from the Amaldi Research Center funded by the MIUR program Dipartimento di Eccellenza (CUP:B81I18001170001) and funding from the INFN TEONGRAV specific initiative. We conduct numerical simulation on XC50 at the Center for Computational Astrophysics (CfCA) of the National Astronomical Observatory of Japan and XC40. We also carry out calculations on XC40 at YITP in Kyoto University. The work was also conducted using the resource of Fujitsu PRIMERGY CX2550M5/CX2560M5(Oakbridge-CX) in the Information Technology Center, The University of Tokyo. We use the SPH visualization tool SPLASH (Price 2007) in Figs. 1 and 5.

DATA AVAILABILITY

The data underlying this article will be shared on reasonable request to the corresponding author.

REFERENCES

- Abbott B. P., et al., 2016, *Physical Review Letters*, **116**, 131103
- Abbott R., Abbott T. D., Abraham S., Acernese F., Ackley K., Adams et al. 2021, *Physical Review X*, **11**, 021053
- Alvarez M. A., Wise J. H., Abel T., 2009, *ApJ*, **701**, L133
- André P., et al., 2010, *A&A*, **518**, L102
- Aykutalp A., Wise J. H., Meijerink R., Spaans M., 2013, *ApJ*, **771**, 50
- Aykutalp A., Wise J. H., Spaans M., Meijerink R., 2014, *ApJ*, **797**, 139
- Ballero S. K., Matteucci F., Chiappini C., 2006, *New Astron.*, **11**, 306
- Bastien P., 1983, *A&A*, **119**, 109
- Bate M. R., 2009, *MNRAS*, **392**, 590
- Bate M. R., 2012, *MNRAS*, **419**, 3115
- Bate M. R., 2019, *MNRAS*, **484**, 2341
- Bate M. R., Burkert A., 1997, *MNRAS*, **288**, 1060
- Bate M. R., Bonnell I. A., Price N. M., 1995, *MNRAS*, **277**, 362
- Bate M. R., Bonnell I. A., Bromm V., 2003, *MNRAS*, **339**, 577
- Belczynski K., Bulik T., Fryer C. L., Ruitter A., Valsecchi F., Vink J. S., Hurley J. R., 2010, *ApJ*, **714**, 1217
- Bonnell I. A., Vine S. G., Bate M. R., 2004, *MNRAS*, **349**, 735
- Bonnell I. A., Clarke C. J., Bate M. R., 2006, *MNRAS*, **368**, 1296
- Bovino S., Grassi T., Schleicher D. R. G., Latif M. A., 2014, *ApJ*, **790**, L35
- Bromm V., Kudritzki R. P., Loeb A., 2001, *The Astrophysical Journal*, **552**, 464
- Caselli P., Benson P. J., Myers P. C., Tafalla M., 2002, *ApJ*, **572**, 238
- Chabrier G., 2003, *PASP*, **115**, 763
- Chiaki G., Yoshida N., 2020, arXiv e-prints, p. arXiv:2008.06107
- Chiaki G., Schneider R., Nozawa T., Omukai K., Limongi M., Yoshida N., Chieffi A., 2014, *MNRAS*, **439**, 3121
- Chiaki G., Marassi S., Nozawa T., Yoshida N., Schneider R., Omukai K., Limongi M., Chieffi A., 2015, *MNRAS*, **446**, 2659
- Chiaki G., Yoshida N., Hirano S., 2016, *MNRAS*, **463**, 2781
- Chiaki G., Susa H., Hirano S., 2018, *MNRAS*, **475**, 4378
- Chiappini C., Matteucci F., Padoan P., 2000, *ApJ*, **528**, 711
- Chon S., Hosokawa T., 2019, *MNRAS*, **488**, 2658
- Chon S., Latif M. A., 2017, *MNRAS*, **467**, 4293
- Chon S., Omukai K., 2020, *MNRAS*, **494**, 2851
- Chon S., Hirano S., Hosokawa T., Yoshida N., 2016, *ApJ*, **832**, 134
- Chon S., Hosokawa T., Yoshida N., 2018, *MNRAS*, **475**, 4104
- Chon S., Hosokawa T., Omukai K., 2021, *MNRAS*, **502**, 700
- Clark P. C., Glover S. C. O., Klessen R. S., 2008, *ApJ*, **672**, 757
- Clark P. C., Glover S. C. O., Klessen R. S., V., 2011, *ApJ*, **727**, 110
- Cunningham A. J., Krumholz M. R., McKee C. F., Klein R. I., 2018, *MNRAS*, **476**, 771
- Dale J. E., Ercolano B., Bonnell I. A., 2012, *MNRAS*, **424**, 377
- De Marchi G., Paresce F., Pulone L., 2007, *ApJ*, **656**, L65
- Dobbs C., Baba J., 2014, *Publ. Astron. Soc. Australia*, **31**, e035
- Dopcke G., Glover S. C. O., Clark P. C., Klessen R. S., 2011, *ApJ*, **729**, L3
- Dopcke G., Glover S. C. O., Clark P. C., Klessen R. S., 2013, *ApJ*, **766**, 103
- Federrath C., Schrön M., Banerjee R., Klessen R. S., 2014, *ApJ*, **790**, 128
- Fukushima H., Omukai K., Hosokawa T., 2018, *MNRAS*, **473**, 4754
- Fukushima H., Hosokawa T., Chiaki G., Omukai K., Yoshida N., Kuiper R., 2020a, *MNRAS*, **497**, 829
- Fukushima H., Yajima H., Sugimura K., Hosokawa T., Omukai K., Matsumoto T., 2020b, *MNRAS*, **497**, 3830
- Geen S., Watson S. K., Rosdahl J., Bieri R., Klessen R. S., Hennebelle P., 2018, *MNRAS*, **481**, 2548
- Ginolfi M., Graziani L., Schneider R., Marassi S., Valiante R., Dell'Agli F., Ventura P., Hunt L. K., 2018, *MNRAS*, **473**, 4538
- Glover S. C. O., 2015, *MNRAS*, **451**, 2082
- Graziani L., Salvadori S., Schneider R., Kawata D., de Bressan M., Maselli A., 2015, *MNRAS*, **449**, 3137
- Graziani L., de Bressan M., Schneider R., Kawata D., Salvadori S., 2017, *MNRAS*, **469**, 1101
- Graziani L., Schneider R., Marassi S., Del Pozzo W., Mapelli M., Giacobbo N., 2020, *MNRAS*, **495**, L81
- Greif T. H., Bromm V., Clark P. C., Glover S. C. O., Smith R. J., Klessen R. S., Yoshida N., Springel V., 2012, *MNRAS*, **424**, 399
- Guszejnov D., Hopkins P. F., Grudić M. Y., Krumholz M. R., Federrath C., 2018, *MNRAS*, **480**, 182
- Hanawa T., Matsumoto T., 2000, *PASJ*, **52**, 241
- Hartwig T., et al., 2018, *MNRAS*, **478**, 1795
- He C.-C., Ricotti M., Geen S., 2019, *MNRAS*, **489**, 1880
- Heger A., Woosley S. E., 2002, *ApJ*, **567**, 532
- Hennebelle P., Banerjee R., Vázquez-Semadeni E., Klessen R. S., Audit E., 2008, *A&A*, **486**, L43
- Heyer M. H., Brunt C. M., 2004, *ApJ*, **615**, L45
- Higuchi K., Machida M. N., Susa H., 2018, *MNRAS*, **475**, 3331
- Hirano S., Hosokawa T., Yoshida N., Umeda H., Omukai K., Chiaki G., Yorke H. W., 2014, *ApJ*, **781**, 60
- Hirano S., Hosokawa T., Yoshida N., Omukai K., Yorke H. W., 2015, *MNRAS*, **448**, 568
- Hirashita H., Omukai K., 2009, *MNRAS*, **399**, 1795
- Hollenbach D., McKee C. F., 1979, *ApJS*, **41**, 555
- Hopkins P. F., 2012, *MNRAS*, **423**, 2016
- Hosokawa T., Omukai K., 2009, *ApJ*, **691**, 823
- Hosokawa T., Omukai K., Yoshida N., Yorke H. W., 2011, *Science*, **334**, 1250
- Hosokawa T., Omukai K., Yorke H. W., 2012, *ApJ*, **756**, 93
- Hosokawa T., Hirano S., Kuiper R., Yorke H. W., Omukai K., Yoshida N., 2016, *ApJ*, **824**, 119
- Inayoshi K., Visbal E., Haiman Z., 2020, *ARA&A*, **58**, 27
- Inoue T., Inutsuka S.-i., 2009, *ApJ*, **704**, 161
- Inoue T., Omukai K., 2015, *ApJ*, **805**, 73
- Inutsuka S.-I., Miyama S. M., 1992, *ApJ*, **388**, 392
- Inutsuka S.-i., Inoue T., Iwasaki K., Hosokawa T., 2015, *A&A*, **580**, A49
- Ishiyama T., Sudo K., Yokoi S., Hasegawa K., Tominaga N., Susa H., 2016, *ApJ*, **826**, 9
- Jappsen A. K., Klessen R. S., Larson R. B., Li Y., Mac Low M. M., 2005, *A&A*, **435**, 611
- Jappsen A.-K., Klessen R. S., Glover S. C. O., Mac Low M.-M., 2009, *ApJ*, **696**, 1065
- Jeon M., Pawlik A. H., Greif T. H., Glover S. C. O., Bromm V., Milosavljević M., Klessen R. S., 2012, *ApJ*, **754**, 34
- Johnson J. L., Bromm V., 2007, *MNRAS*, **374**, 1557
- Johnson J. L., Khochfar S., Greif T. H., Durier F., 2011, *MNRAS*, **410**, 919
- Johnson J. L., Dalla V. C., Khochfar S., 2013, *MNRAS*, **428**, 1857
- Kalari V. M., Rubio M., Saldaña H. P., Bolatto A. D., 2020, *MNRAS*, **499**, 2534
- Kinugawa T., Inayoshi K., Hotokezaka K., Nakauchi D., Nakamura T., 2014, *MNRAS*, **442**, 2963
- Kitsionas S., Whitworth A. P., 2002, *MNRAS*, **330**, 129
- Koh D., Wise J. H., 2016, *MNRAS*, **462**, 81
- Könyves V., et al., 2015, *A&A*, **584**, A91
- Koyama H., Inutsuka S.-i., 2002, *ApJ*, **564**, L97
- Kroupa P., 2002, *Science*, **295**, 82
- Krujissen J. M. D., 2014, *Classical and Quantum Gravity*, **31**, 244006

- Krumholz M. R., Klein R. I., McKee C. F., 2012, *ApJ*, **754**, 71
- Krumholz M. R., McKee C. F., Bland-Hawthorn J., 2019, *ARA&A*, **57**, 227
- Kuruwita R. L., Federrath C., Ireland M., 2017, *MNRAS*, **470**, 1626
- Larson R. B., 1969, *MNRAS*, **145**, 271
- Larson R. B., 1981, *MNRAS*, **194**, 809
- Larson R. B., 1985, *MNRAS*, **214**, 379
- Larson R. B., 1998, *MNRAS*, **301**, 569
- Larson R. B., 2005, *MNRAS*, **359**, 211
- Latif M. A., Schleicher D. R. G., Schmidt W., Niemeyer J. C., 2013, *MNRAS*, **436**, 2989
- Lee Y. S., Suda T., Beers T. C., Stancliffe R. J., 2014, *ApJ*, **788**, 131
- Li Y., Klessen R. S., Mac Low M.-M., 2003, *ApJ*, **592**, 975
- Lipovka A., Núñez-López R., Avila-Reese V., 2005, *MNRAS*, **361**, 850
- Mac Low M.-M., 1999, *ApJ*, **524**, 169
- Machida M. N., Doi K., 2013, *MNRAS*, **435**, 3283
- Machida M. N., Nakamura T., 2015, *MNRAS*, **448**, 1405
- Machida M. N., Inutsuka S.-i., Matsumoto T., 2008a, *ApJ*, **676**, 1088
- Machida M. N., Matsumoto T., Inutsuka S.-i., 2008b, *ApJ*, **685**, 690
- Machida M. N., Omukai K., Matsumoto T., Inutsuka S.-I., 2009, *MNRAS*, **399**, 1255
- Machida M. N., Inutsuka S.-I., Matsumoto T., 2011, *PASJ*, **63**, 555
- Magg M., Hartwig T., Agarwal B., Frebel A., Glover S. C. O., Griffen B. F., Klessen R. S., 2018, *MNRAS*, **473**, 5308
- Marassi S., Graziani L., Ginolfi M., Schneider R., Mapelli M., Spera M., Alparone M., 2019, *MNRAS*, **484**, 3219
- Marks M., Kroupa P., Dabringhausen J., Pawlowski M. S., 2012, *MNRAS*, **422**, 2246
- Marsh K. A., et al., 2016, *MNRAS*, **459**, 342
- Martinelli A., Matteucci F., 2000, *A&A*, **353**, 269
- Masunaga H., Inutsuka S.-i., 2000, *ApJ*, **531**, 350
- Mathis J. S., Rumpl W., Nordsieck K. H., 1977, *ApJ*, **217**, 425
- Matsukoba R., Takahashi S. Z., Sugimura K., Omukai K., 2019, *MNRAS*, **484**, 2605
- Matsushita Y., Sakurai Y., Hosokawa T., Machida M. N., 2018, *MNRAS*, **475**, 391
- Mayer M., Duschl W. J., 2005, *MNRAS*, **358**, 614
- McKee C. F., Tan J. C., 2003, *ApJ*, **585**, 850
- McKee C. F., Tan J. C., 2008, *ApJ*, **681**, 771
- Meece G. R., Smith B. D., O'Shea B. W., 2014, *ApJ*, **783**, 75
- Mellon R. R., Li Z.-Y., 2008, *ApJ*, **681**, 1356
- Myers A. T., Krumholz M. R., Klein R. I., McKee C. F., 2011, *ApJ*, **735**, 49
- Myers A. T., McKee C. F., Cunningham A. J., Klein R. I., Krumholz M. R., 2013, *ApJ*, **766**, 97
- Myers A. T., Klein R. I., Krumholz M. R., McKee C. F., 2014, *MNRAS*, **439**, 3420
- Nakatani R., Fialkov A., Yoshida N., 2020, *ApJ*, **905**, 151
- Nozawa T., Kozasa T., Umeda H., Maeda K., Nomoto K., 2003, *ApJ*, **598**, 785
- Nozawa T., Kozasa T., Nomoto K., 2012, *ApJ*, **756**, L35
- Omukai K., 2000, *ApJ*, **534**, 809
- Omukai K., Nishi R., 1998, *ApJ*, **508**, 141
- Omukai K., Palla F., 2003, *ApJ*, **589**, 677
- Omukai K., Tsuribe T., Schneider R., Ferrara A., 2005, *ApJ*, **626**, 627
- Omukai K., Hosokawa T., Yoshida N., 2010, *ApJ*, **722**, 1793
- Peters P. C., 1964, *Phys. Rev.*, **136**, B1224
- Peters T., Klessen R. S., Mac Low M.-M., Banerjee R., 2010, *ApJ*, **725**, 134
- Price D. J., 2007, *Publ. Astron. Soc. Australia*, **24**, 159
- Regan J. A., Visbal E., Wise J. H., Haiman Z., Johansson P. H., Bryan G. L., 2017, *Nature Astronomy*, **1**, 0075
- Riaz R., Schleicher D. R. G., Vanaverbeke S., Klessen R. S., 2020, *MNRAS*, **494**, 1647
- Ripamonti E., 2007, *MNRAS*, **376**, 709
- Ritter J. S., Sluder A., Safrank-Shrader C., Milosavljević M., Bromm V., 2015, *MNRAS*, **451**, 1190
- Sadanari K. E., Omukai K., Sugimura K., Matsumoto T., Tomida K., 2021, *MNRAS*, **505**, 4197
- Safrank-Shrader C., Milosavljević M., Bromm V., 2014, *MNRAS*, **438**, 1669
- Safrank-Shrader C., Montgomery M. H., Milosavljević M., Bromm V., 2016, *MNRAS*, **455**, 3288
- Salpeter E. E., 1955, *ApJ*, **121**, 161
- Salvadori S., Schneider R., Ferrara A., 2007, *MNRAS*, **381**, 647
- Salvadori S., Ferrara A., Schneider R., 2008, *MNRAS*, **386**, 348
- Schleicher D. R. G., Banerjee R., Sur S., Arshakian T. G., Klessen R. S., Beck R., Spaans M., 2010, *A&A*, **522**, A115
- Schneider R., Omukai K., 2010, *MNRAS*, **402**, 429
- Schneider R., Ferrara A., Salvaterra R., Omukai K., Bromm V., 2003, *Nature*, **422**, 869
- Schneider R., Ferrara A., Salvaterra R., 2004, *MNRAS*, **351**, 1379
- Schneider R., Omukai K., Inoue A. K., Ferrara A., 2006, *MNRAS*, **369**, 1437
- Schneider R., Omukai K., Bianchi S., Valiante R., 2012, *MNRAS*, **419**, 1566
- Schneider R., Graziani L., Marassi S., Spera M., Mapelli M., Alparone M., Bressan M. d., 2017, *MNRAS*, **471**, L105
- Schober J., Schleicher D., Federrath C., Glover S., Klessen R. S., Banerjee R., 2012, *ApJ*, **754**, 99
- Semenov D., Henning T., Helling C., Ilgner M., Sedlmayr E., 2003, *A&A*, **410**, 611
- Shima K., Hosokawa T., 2021, arXiv e-prints, p. arXiv:2102.06312
- Shu F. H., 1977, *ApJ*, **214**, 488
- Sluder A., Ritter J. S., Safrank-Shrader C., Milosavljević M., Bromm V., 2016, *MNRAS*, **456**, 1410
- Smith B. D., Sigurdsson S., 2007, *ApJ*, **661**, L5
- Smith R. J., Glover S. C. O., Clark P. C., Greif T., Klessen R. S., 2011, *MNRAS*, **414**, 3633
- Smith B. D., Wise J. H., O'Shea B. W., Norman M. L., Khochfar S., 2015, *MNRAS*, **452**, 2822
- Spera M., Mapelli M., Giacobbo N., Trani A. A., Bressan A., Costa G., 2019, *MNRAS*, **485**, 889
- Springel V., 2005, *MNRAS*, **364**, 1105
- Stacy A., Greif T. H., Klessen R. S., Bromm V., Loeb A., 2013, *MNRAS*, **431**, 1470
- Stacy A., Bromm V., Lee A. T., 2016, *MNRAS*, **462**, 1307
- Stone J. M., Ostriker E. C., Gammie C. F., 1998, *ApJ*, **508**, L99
- Suda T., et al., 2013, *MNRAS*, **432**, L46
- Sugimura K., Matsumoto T., Hosokawa T., Hirano S., Omukai K., 2020, *ApJ*, **892**, L14
- Susa H., 2019, *ApJ*, **877**, 99
- Susa H., Hasegawa K., Tominaga N., 2014, *ApJ*, **792**, 32
- Tanaka K. E. I., Omukai K., 2014, *MNRAS*, **439**, 1884
- Tanaka H., Takeuchi T., Ward W. R., 2002, *ApJ*, **565**, 1257
- Tinsley B. M., 1980, *Fundamentals Cosmic Phys.*, **5**, 287
- Todini P., Ferrara A., 2001, *MNRAS*, **325**, 726
- Truelove J. K., Klein R. I., McKee C. F., Holliman II J. H., Howell L. H., Greenough J. A., 1997, *ApJ*, **489**, L179
- Tsuribe T., Omukai K., 2006, *ApJ*, **642**, L61
- Valiante R., Schneider R., Volonteri M., Omukai K., 2016, *MNRAS*, **457**, 3356
- Walch S. K., Whitworth A. P., Bisbas T., Wünsch R., Hubber D., 2012, *MNRAS*, **427**, 625
- Wise J. H., Turk M. J., Norman M. L., Abel T., 2012, *ApJ*, **745**, 50
- Wise J. H., Regan J. A., O'Shea B. W., Norman M. L., Downes T. P., Xu H., 2019, *Nature*, **566**, 85
- Yoshida N., Omukai K., Hernquist L., 2008, *Science*, **321**, 669

de Bennassuti M., Schneider R., Valiante R., Salvadori S., 2014, [MNRAS](#), **445**, 3039

de Bennassuti M., Salvadori S., Schneider R., Valiante R., Omukai K., 2017, [MNRAS](#), **465**, 926